Sedimentary heterogeneity and petrophysical characterization of Barremian tsunami and barrier island/inlet deposits: the Aliaga outcrop as a reservoir analogue (Galve Sub-Basin, eastern Spain).

F. M. L. Veloso* (1), R. Navarrete (1), A.R. Soria (1) and N. Meléndez (2)

(1) Departamento de Ciencias de la Tierra (Universidad de Zaragoza). C/ Pedro Cerbuna 12, 50009, Zaragoza. Spain.

(2) Departamento de Estratigrafía (Fac. Geología, Universidad Complutense de Madrid). José Antonio Novais, 2; 28040, Madrid, Spain. Instituto de Geociencias (IGEO), UCM, CSIC.

* Corresponding author: e-mail (permanent address): fe_geo@hotmail.com. Phone: 0033 628 34 85 56.

Abstract

The present study examined two sandstone deposits in the Aliaga outcrop as a reservoir analogue over a distance of 200-m-long and attempted to establish a correlation between sand facies and the petrophysical properties of the sandstones in order to investigate the reservoir heterogeneity. The Aliaga reservoir analogue represents the upper part of Camarillas Fm., deposited during the Barremian synrift phase of the Galve sub-basin (Iberian Basin, Spain). It is characterized by a transitional sedimentary interval from sandy-dominant deposits to carbonate-dominant deposits, which were deposited under the same palaeoenvironmental conditions (in relation to systems of back-barrier sedimentation).

The description of the Aliaga outcrop provided here consists of lithological descriptions of two sandstone deposits: a tsunami and a barrier island/inlet, at both mesoscopic (decimeters to tens of meters) and microscopic scales (millimeters to centimeters). Both deposits recognized at the basin scale were described in terms of sand grain size, sand sorting and

cementation; further cores were drilled along outcrop to collect samples for porosity and permeability measurements.

Both sandstone reservoirs are the result of different sedimentary processes that determined facies characteristics, as the different petrophysical properties observed in these deposits. Consequently, the sedimentary process controls the heterogeneity of the sandstones facies and thus, the sand heterogeneity controls the distribution of the petrophysical properties. The classification of sand facies in terms of sand sorting seems to be more appropriate for describing sand heterogeneity; accordingly, petrophysical parameters in both deposits were also influenced by sand sorting.

The sand facies and petrophysics heterogeneity of the described deposits can be hierarchically ordered. First-order heterogeneity is related to the basin scale, second-order heterogeneity is related to genesis and the conditions of sediment deposition, and third-order heterogeneity is related to synsedimentary faults and/or post-sedimentation events.

Keywords

Reservoir analogue; tsunami; barrier island-inlet; heterogeneity; sand facies, porosity; permeability; sand sorting.

1. Introduction

Sedimentary heterogeneity on sandstone deposits depends on the scale and the phenomenon that is been investigated (Cushman, 1997; Bachu *et al.* 2007; Frykman, 2009). The sedimentary heterogeneity into reservoir models are usually expressed by the distribution of low-permeability structural or diagenetic features, such as faults, breccia or deformation bands (Eaton, 2006), or by the attribution of low-permeability facies, such as mud drapes or

shale layers (Ashraf, 2014; Issautier *et al.* 2014). However, detailed studies on outcrops have showed the impact of the textural features of the reservoir sandstone, such as grain-size distribution, sorting index, net to gross (percentage of clay and/or silt) and rock texture, on the spatial distribution of the petrophysical properties, such as porosity, permeability or capillarity entry pressure (Hornung and Aigner, 1999; Klingbeil *et al.* 1999; Heinz, *et al.*, 2003; Sun *et al.*, 2007; Ambrose *et al.* 2008; Huysmans *et al.*, 2008; Frykman *et al.* 2013).

The challenge in building geological models for reservoir studies is the integration of different scales of heterogeneity with the most relevant petrophysic characteristics that impact the fluid flow into the reservoir (Corbett and Potter, 2004). The high resolution of sedimentary heterogeneity of reservoir or groundwater models improves the accuracy for prediction the behaviour of fluid flow, principally in clastic sedimentary systems where petrophysical parameters (porosity and/or permeability) are commonly correlated with specific sandy lithofacies (Hornung and Aigner, 1999; Heinz *et al.*, 2003; Huysmans *et al.*, 2008; Norden *et al.*, 2010, Pyrcz and Deutsch, 2014). Reservoir models are often constructed at the field scale (from tens to hundreds of square kilometres) and practical limits on the size of reservoir models for post-studies of flow simulation are often imposed (AAPG wiki). The outcrop scale is a bridge between seismic and core scales, as the outcrop represents the scale of individual bedforms (meter to hundred of meters) and laminae (millimetre to meter) (Yoshida *et al.*, 2001).

Sedimentary heterogeneity at the outcrop scale provides access to observe rock with relatively straightforward observation and sampling and with the large-scale features limited by the extent of the outcrop exposure (Pyrcz and Deutsch, 2014). The geomodel built from outcrop provides the reservoir and top seal heterogeneity and architecture, which is necessary to investigate the dynamic influence of the main intra-body heterogeneities into

reservoir flow-simulation studies (Robinson and McCabe, 1997; Dalrymple, 2001; Tye, 2004; Wood, 2004; Ekeland *et al.*, 2008). Therefore, analogous outcrop studies supply detailed geological information that can help to elucidate the geological gaps of local zones in the reservoir model, as well as they should be useful in defining the spatial variability of reservoir properties (White *et al.*, 2004). There are some significant limitations to outcrop information. Firstly, the data is typically 2-D (Lantuéjoul *et al.*, 2005) and present some observational bias. Consolidated rock is often preserved in outcrop while less-consolidated rocks (e.g., shales) are eroded and, if dominant, prevent the formation of outcrops in the first place. Also, weathering and unloading of the rocks may change the outcrop exposure and obscure observation of features relevant in the in situ state (Pyrcz and Deutsch, 2014).

This study attempts to investigate the correlation between the characteristics of sandy facies and their petrophysical parameters, such as porosity and permeability, at the outcrop scale in the Aliaga reservoir analogue (Early Cretaceous Galve Sub-Basin, eastern Spain, Fig. 1). Two sandstone bodies were the main targets of this study. They deposited under the same palaeogeographical context but in relation to different sedimentary processes, one representing a tsunami deposit and the other a barrier-island/inlet deposit. Both deposits were studied in detail at both mesoscopic (metre to hundred of metres) and microscopic (millimetre to centimetres) scales for identifying heterogeneities in relation with the different involved sedimentary facies. Porosity and permeability measurements were made for the different sandy facies and results are compared and discussed in the context of the sedimentary processes involved during deposition in each deposit. A discussion on the different orders of heterogeneity and their control is also included.

2. Geological setting

The Aliaga outcrop of the Barremian Camarillas Fm. studied as reservoir analogue is located in the Cretaceous Galve sub-basin, which is situated in the Iberian Chain, in central–eastern Iberia (Fig. 1A). The NNW–SSE elongate Galve sub-basin (40 km long and 20 km wide) was a western marginal sedimentation area of the Maestrazgo Basin, which was developed during the Late Jurassic–Early Cretaceous rifting that affected Iberia (e.g., Salas and Casas, 1993; Capote *et al.*, 2002; Antolín-Tomas *et al.*, 2007). The activity of two main fault sets, one trending NNW–SSE (e.g. the Alpeñés, Ababuj, Cañada Vellida, and Miravete faults) and the other trending ENE–WSW (the Campos, Santa Bárbara, Aliaga, Camarillas and Remenderuelas faults) (Fig. 1B) determined the Early Cretaceous extensional structure of the Galve sub-basin (Soria 1997; Liesa *et al.*, 2000; Soria *et al.*, 2001; Navarrete *et al.*, 2013a, 2014).

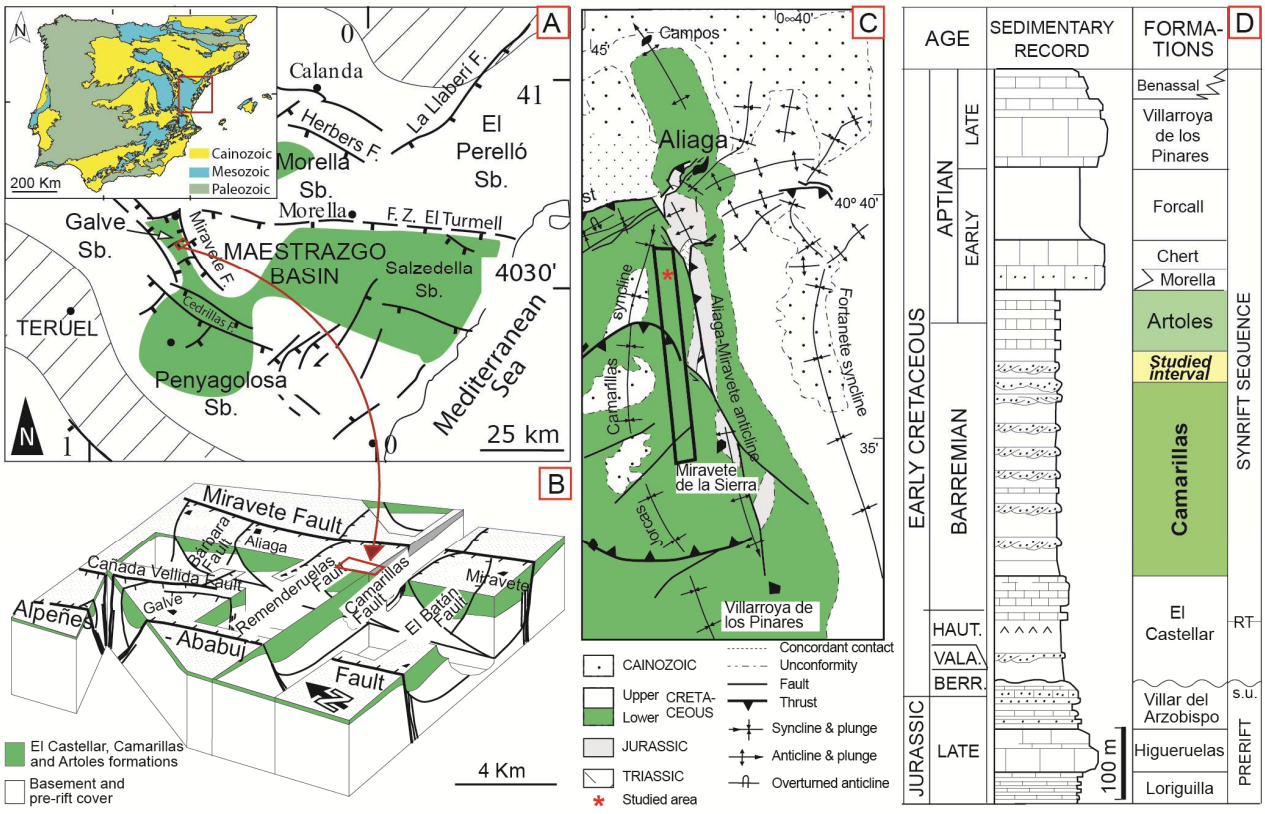

Fig. 1: Geological setting of the studied outcrop analogue in the Galve sub-basin (modified from Navarrete *et al.* 2013a). (A) Location of the Maestrazgo Basin and the Galve sub-basin; the area shown in Fig. 2 is highlighted by the red square (modified from Capote *et al.*, 2002). (B) Block diagram showing the

tectonic setting of the Galve sub-basin during deposition of the El Castellar, Camarillas and Artoles formations (modified from Liesa *et al.*, 2006). (C) Close-up of the area highlighted in Fig. 2 and location of the outcrop between the Aliaga–Miravete Anticline and the Camarillas–Jorcas Syncline. (D) Chronostratigraphic diagram and sedimentary record of the Galve sub-basin and the studied interval (s.u., synrift unconformity; RT, rift transition) (modified from Rodríguez-López *et al.*, 2009).

The structure of the studied region shows the superimposition of two mainly Palaeogene, orthogonal fold-and-thrust structural trends, one striking NNW–SSE (e.g., Aliaga-Miravete Anticline, Camarillas-Jorcas Syncline, Fig. 1C), and the other WSW–ENE (Camarillas and Remenderuelas faults, Fig. 2). Both structural trends represent the rejuvenation and inversion of normal faults, basically inherited from Mesozoic extensional and/or post-Variscan fracturing (Guimerà *et al.*, 1996; Soria, 1997; Liesa *et al.*, 2004, 2006). Present-day morphotectonics are the result of extensional deformation that began on the eastern margin of the Iberian Peninsula during the mid-Miocene, related to rifting in the Valencia Trough (Álvaro *et al.*, 1979).

Synrift sedimentation in the Galve sub-basin spans the late Hauterivian to the early Albian (Soria, 1997; Soria *et al.*, 2000; Salas *et al.*, 2001; Liesa *et al.*, 2004, 2006; Peropadre, 2012), and comprises the following units (Fig. 1D): (1) an alluvial and lacustrine series (El Castellar Fm.; Soria, 1997) that records the transition from initial rifting to rift climax (Liesa *et al.*, 2006; Meléndez *et al.*, 2009); (2) red clays and sandstones (Camarillas Fm.) recently interpreted as deposited in a transitional continental-to-marine sedimentary system. This transitional system is composed of tidal mud flat with tidal channel deposits at the base, changing upward into barrier island and lagoon deposits (Navarrete, 2015); (3) marls and limestones (Artoles Fm.) rich in calcareous algae, planktonic foraminifera and molluscs, interpreted as a shallow marine to transitional carbonate system (Salas, 1987; Soria, 1997); (4) a series of siliciclastic and/or carbonate marine platforms (Morella, Chert, Forcall,

Villarroya de los Pinares and Benasal Fm.) characteristic of Aptian sedimentation (e.g., Vennin and Aurell, 2001; Peropadre *et al.*, 2008; Peropadre, 2012); and (5) a late Aptian–early Albian transitional siliciclastic series with coal beds (Escucha Fm.; Rodríguez-López *et al.*, 2009).

The studied sediments belong to the Camarillas Fm., which constitutes one of the most important thickest sedimentary units to be deposited in the Galve sub-basin during the Barremian synrift phase (Soria, 1997) (Figs. 1D and 2). This unit exhibits large thickness variations (150–800 m) that are related to extensional faulting (Soria, 1997; Navarrete *et al.*, 2013a, b; Navarrete, 2015) that occurred at the climax of Cretaceous rifting (Liesa *et al.*, 2004, 2006; Navarrete *et al.*, 2013a).

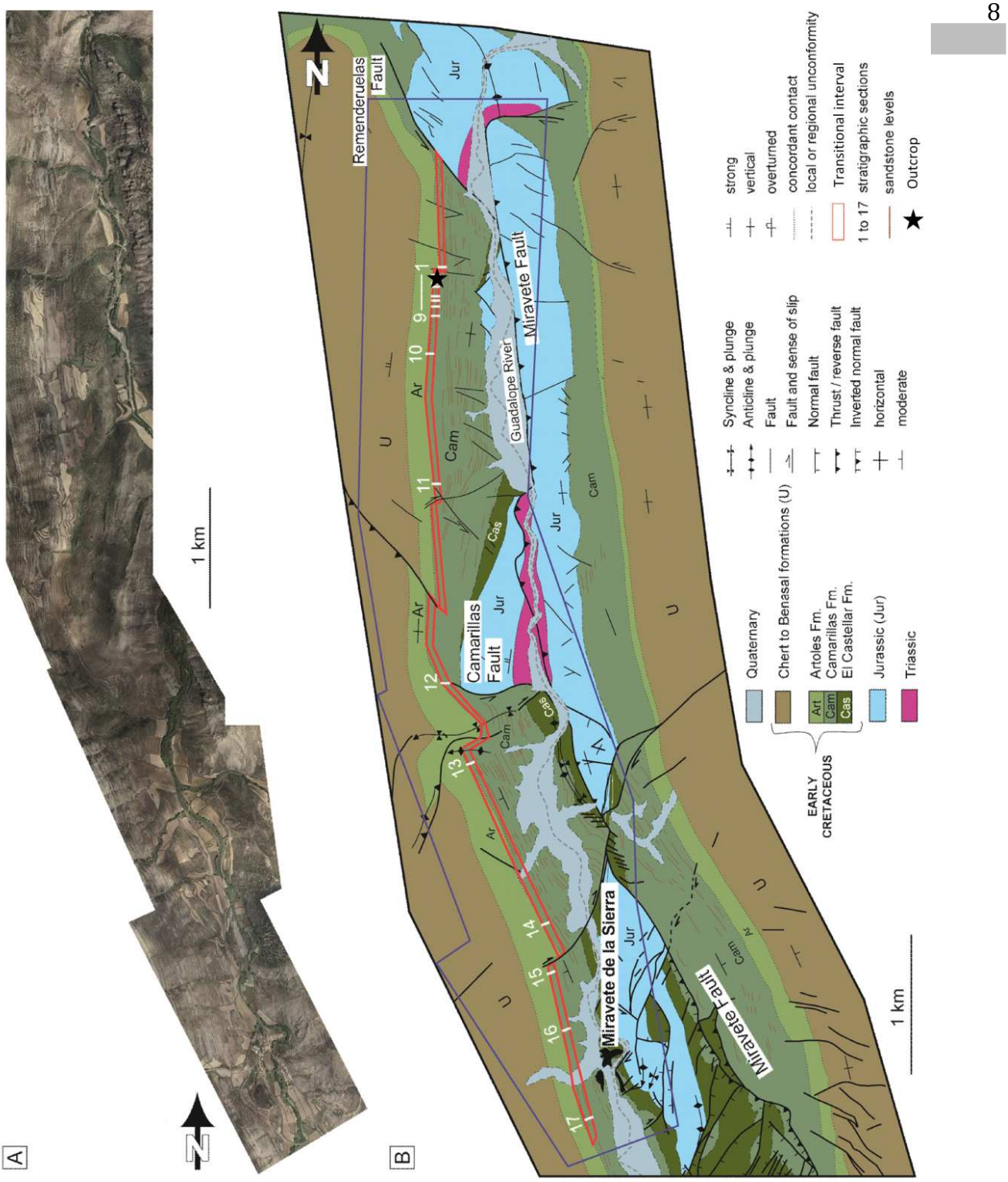

Fig. 2 The Aliaga–Miravete anticline and the Galve sub-basin sedimentary infill. (A) High-resolution satellite image at a scale of 1:5000 (available on the SITAR web page of the Aragón Government). (B) Geological map of Galve sub-basin units across WSW–ENE-striking listric faults; the transitional interval and the outcrop locations are marked, as are the locations of stratigraphic profiles. Modified from Navarrete *et al.* (2013a).

Concretely, the studied sediments in the Aliaga outcrop are included into the upper part of the Camarillas Fm., in a transition interval with the uppermost Artoles Fm. In this interval,

Navarrete *et al.* (2013a) distinguish two stages of back-barrier sedimentation (Figs. 2 and 3). Stage 1 is characterised by extensive back-barrier mud flat deposits, with tidal creeks and minor washover fans, interbedded with lagoonal carbonates; while Stage 2 includes washover fan deposits interbedded with lagoonal carbonates, well-developed ebb- and flood-tidal deposits and the complete absence of back-barrier tidal mud flats and associated channels.

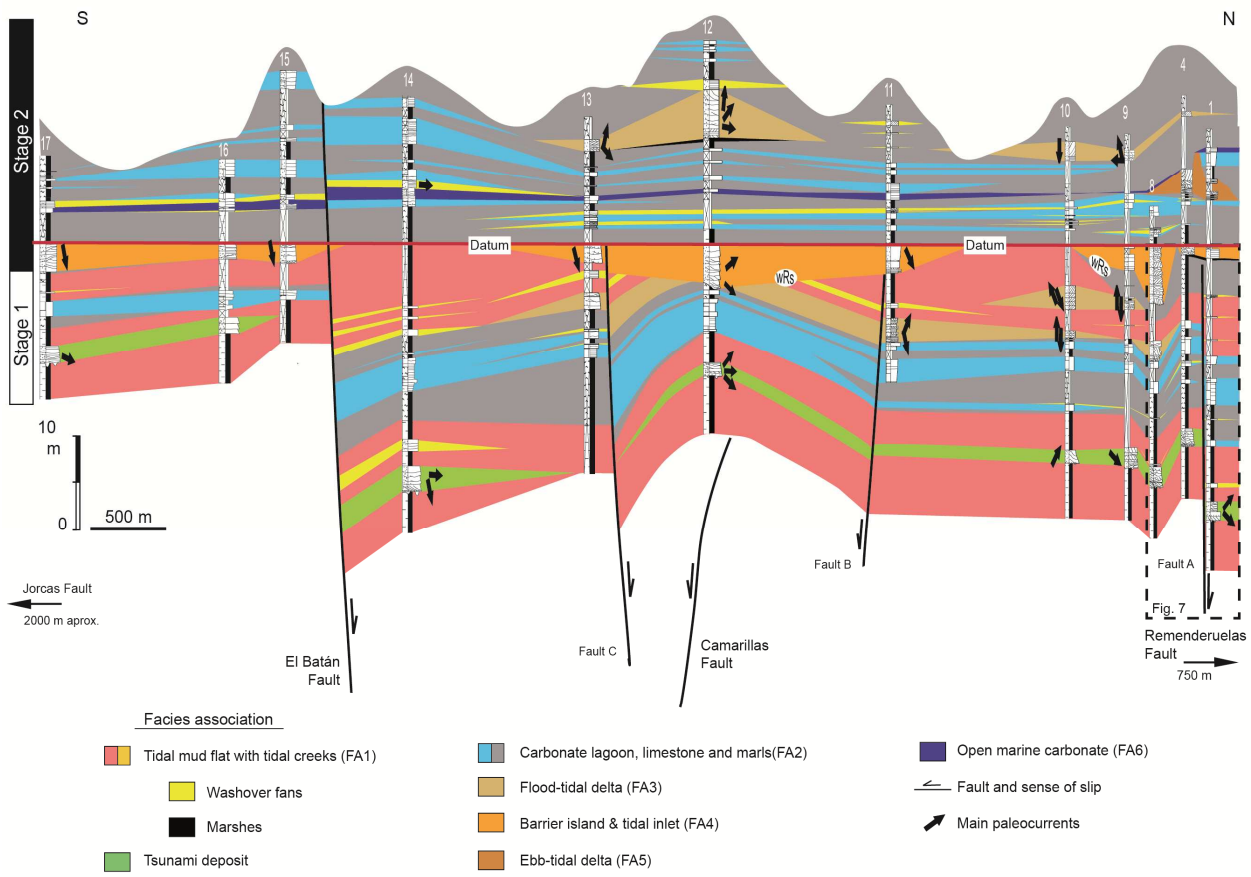

Fig. 3: Sedimentary correlation panel of the transitional interval between the Camarillas Fm. and Artoles Fm. (Fig. 2) with descriptions of facies associations. The sedimentary datum is the barrier island and tidal inlet deposit with a wave ravinement (wRs) surface at the base. Modified from Navarrete *et al.* (2013a).

Below the stage 1 sediments, an exceptional tsunami deposit (up to 3 m thick) has been identified and studied in detail by Navarrete *et al.* (2014). Its is a multiple-bed deposit made

of sandstones and, locally, conglomerates that shows some fining-upwards facies successions sequences, which correspond to incursions and outflows of the tsunami wave train (Fujiwara, 2008; Navarrete *et al.*, 2014). The tsunami sediments accumulated on onshore back-barrier mudflats with lagoon deposits covering and filling exceptionally dinosaur footprints (described below).

3. Materials and methods

This study is mainly based on five detailed sedimentary sections logged along the Aliaga outcrop (see **Error! Reference source not found.** and 4), and located on the aerial photograph of Villarluengo 543-12 (scale, 1:5000). Based on the geographic references of sedimentary sections and the aerial photo, a low aerial photograph of the Aliaga outcrop, obtained by a camera fixed to a drone (unmanned aerial vehicle), was georeferenced to the ED-50 UTM-30 geographic coordinate projection system. Sedimentary interpretations and analysis of drone photographs, previous descriptions of facies associations provided by Navarrete *et al.* (2013a and 2014), and field survey allowed (i) the development of a sampling schema to systematically collect samples for petrographic analyses and petrophysical measurements according to lithological variations, and (ii) to provide upcoming geostatistically analysis.

The Aliaga outcrop was divided into two sectors, the North sector and the South sector, separated by the Aliaga–Miravete road (Fig. 4). In overall, 53 samples were collected at regularly spaced intervals along two sandstone bodies, the tsunami and the barrier island/inlet (b.i./inlet) deposits. In areas where such deposits are thicker than 1 m, several samples were collected, which were located at the base, middle and top of each bed. Samples were extracted using a portable rock core drill (Pomeroy D026-GT10 Gear-Reduced Core Drill with a 48 cm^3 Stihl motor) and a 4" (10 cm) outer-diameter drill bit (BS-4Pro). Orientations of

the extracted cores were measured; their dimensions varied from 10 to 20 cm in length and 8 to 9.5 cm in diameter. The cores were obtained parallel to the dip direction, and were taken on the outcrop face due to constraints imposed by the orientation of the outcrop; therefore core lengths correspond to bed width (Veloso *et al.*, 2013). Samples were taken from each core for petrographic and petrophysical analyses.

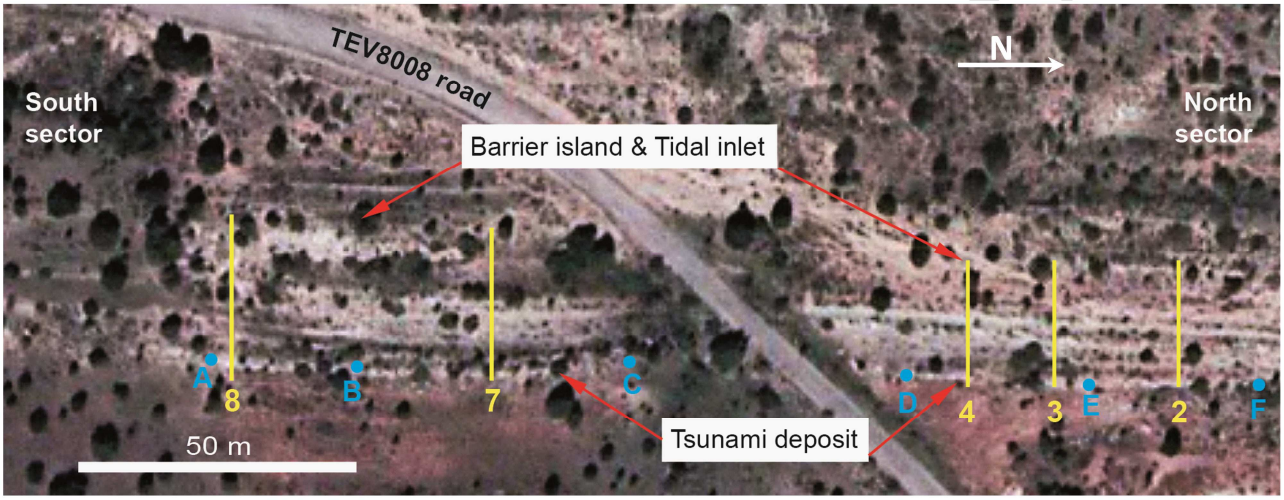

Fig. 4: Aerial photograph of Aliaga outcrop, supplied by the Aragon Visor 2D (http://sitar.aragon.es/) with the location of the Tsunami deposit and barrier-island and inlet deposit, as well as the sedimentary sections 2, 3, 4, 7 and 8 of Fig. 7. The blue points (A, B, C, D, E and F) at the Tsunami deposit are the points to construct the panorama photos in Fig. 13.

Lithofacies described in the field were refined by petrographic descriptions of 65 thin sections, which were made from samples collected from core and hand specimens. Thin sections were oriented perpendicular to bedding, and were chemically stained to identify carbonate. The classification used for the mineralogical analyses was based on that of Pettijohn (1973). Petrographical characterization of samples included the analysis of the grain-size distribution, sorting, shape and nature of grains, matrix components, sedimentary structures and the presence of fossils or cement. Many samples could not be dissolved or

disaggregated by conventional methods used for sedigraph grain-size distribution analyses due to the high concentrations of carbonate clasts and fractured quartz grains; therefore, grain-size distributions, estimates of sand sorting and sand nature were obtained by quick petrographic observations according to a reference chart (U.S. GeoSupply Inc., 2015).

The petrophysical measurements included estimations of sample porosity and permeability by direct measurements on plugs. Fifty-six plugs were taken from the cores for measurements of porosity (Phi) and horizontal permeability (Kh); a further 23 plugs were used for measurements of vertical permeability (Kv). The petrophysical measurements were conducted at the Petrophysics Institute Foundation (IPF), Madrid, Spain, on plugs 60 mm long and 40 mm in diameter. The plugs were cut from the cores as shown in Fig. 5, where the vertical plugs were taken perpendicular to the strike direction or in the North direction, and the horizontal plugs were taken parallel to the strike direction or the North direction. Porosity was estimated by a helium pycnometer at atmospheric conditions and ambient temperatures through gas displacement inside a known cell volume; the pore volume was obtained according to Boley's law (IPF, 2012). The horizontal (Kh) and vertical (Kv) permeabilities were estimated using a gas permeameter at steady-state conditions; the gas permeability was calculated according to Darcy's law and was then corrected to the equivalent liquid permeability using the Klikenberg correction factor (IPF, 2012).

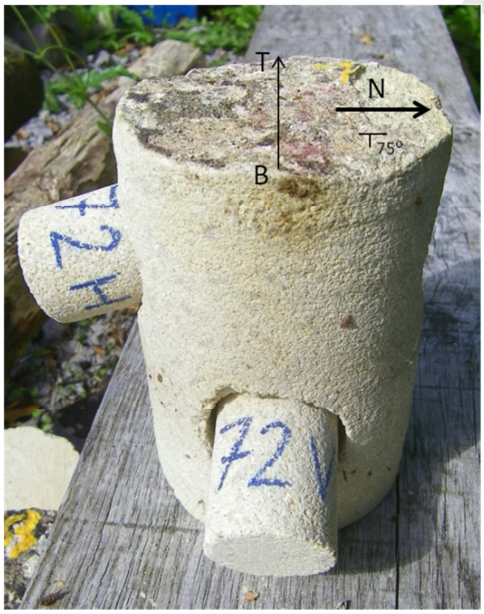

Fig. 5: Core sample and obtained plugs for petrophysical measurements. The core length is parallel to the width of deposit (E-W original direction); "V" plugs were used to measure the vertical permeability and "H" plugs were used to measure the horizontal permeability. Note the orientation of core sample (N points to the North and core had a 75º inclination to

the west, i.e. parallel to the 75º west-dipping sandstone bed) and the position of the vertical and horizontal plugs (B and T indicate base and top of sandstone deposit, respectively)

4. Geology at the outcrop scale: the Aliaga outcrop

The Aliaga outcrop is a 2D face of 210 m wide and 40 m high located on road TEV 8008, 5 km from Aliaga village. This road divides the outcrop into a North sector (on the north side of the road) and a South sector (on the south side of the road) (Fig. 4). This outcrop is located on the steeply dipping (>75°) western limb of the NNW–SSE-trending Aliaga–Miravete anticline, between the ENE–WSW-striking Remenderuelas and Camarillas listric faults (Fig. 2). The Aliaga outcrop studied as analogue comprises from the bottom surface of the tsunami deposit to the top surface of the barrier-island and tidal inlet (b.i./inlet) deposit (Fig. 3). Five sedimentary sections logged by Navarrete et al. (2013a and 2014) are included within the Aliaga outcrop (sections 2, 3, 4, 7 and 8 in Fig. 4). A general sedimentological section is showed in Fig. 6. Though the facies associations distinguished by Navarrete *et al.* (2013a, 2014) were defined taking into account the sedimentary characteristics observed at km-scale, they are also recognized at the Aliaga outcrop (Fig. 7). Brief descriptions of these facies associations are given below.

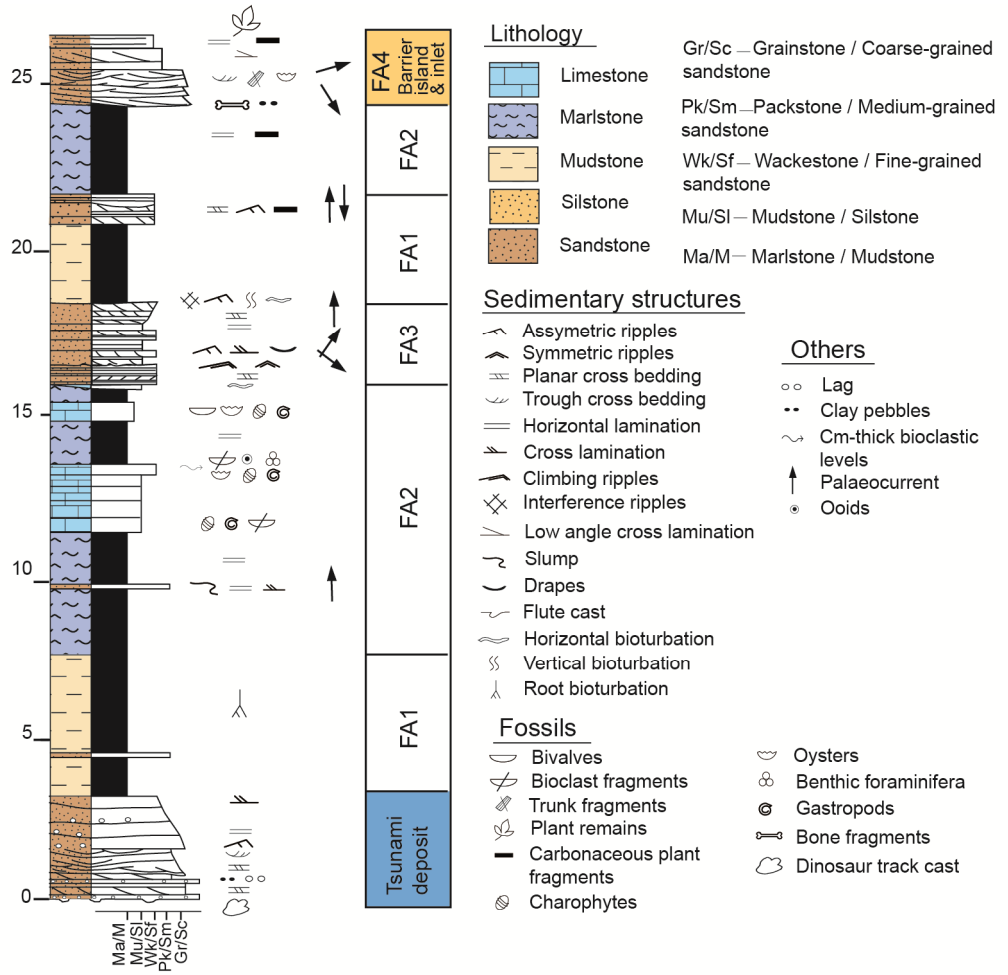

Fig. 6: Schematic sedimentary section of the study interval (modified from Navarrete *et al.*, 2013a).

(A) Tsunami deposit (Figs. 6 and 7). It is a 1 to 5 m thick sandstone body lying on a clay layer bearing dinosaur trackways (including a 7-km-long dinosaur megatracksite). This deposit consists of coarse-, middle-, and fine-grained sandstones, and local mud layers; and several fining upwards facies successions have been observed. In its lower part, a few cm-thick beds of conglomerate with carbonate clasts appear. This deposit is also characterized by its great lateral extent and uniformity in comparison with other facies associations of the island-barrier sedimentary system (Navarrete et al., 2014). See below for a detailed description of the different lithofacies.

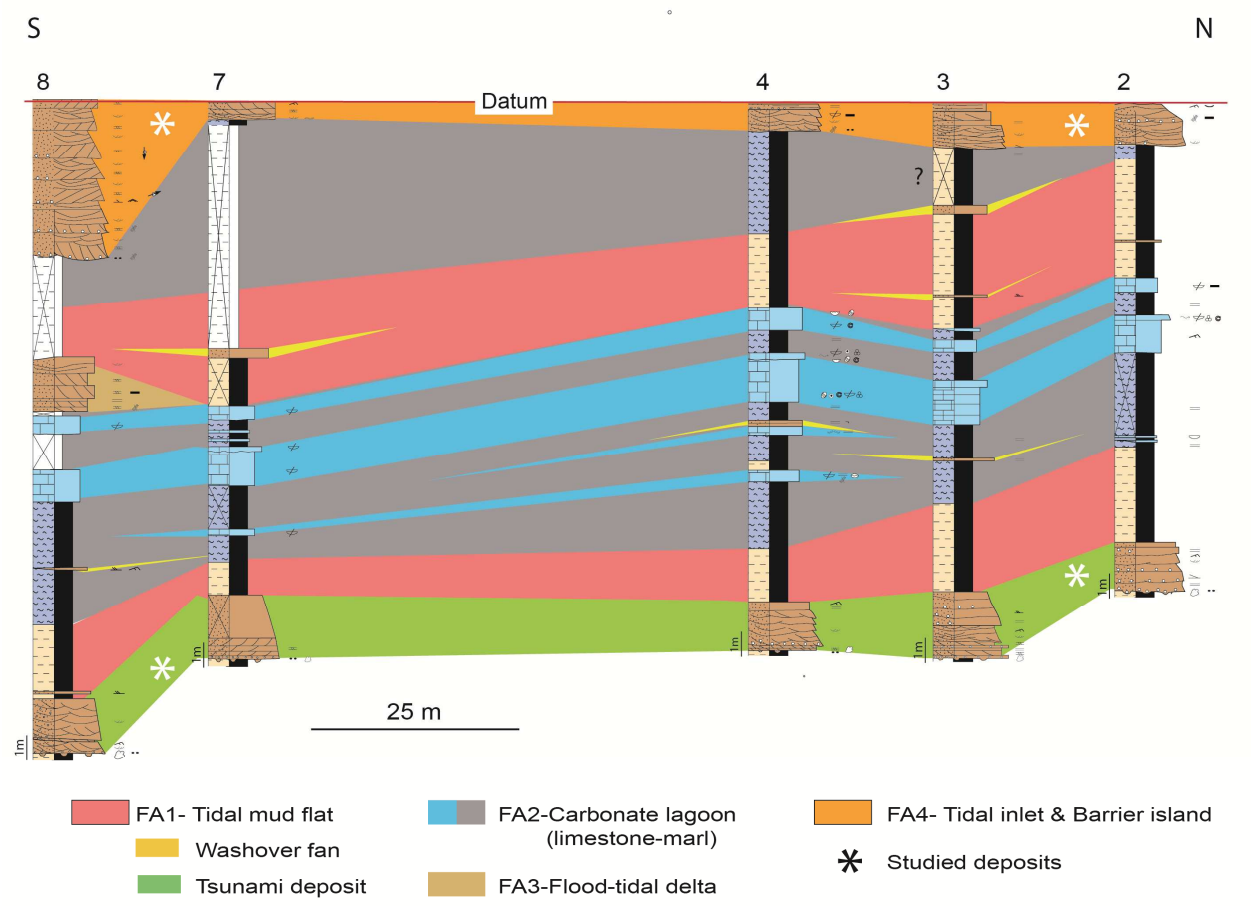

Fig. 7: Detail of sedimentary sections logged at the Aliaga outcrop face, showing the lateral extension of the facies associations identified (see location in Fig. 3).

(B) Tidal mud flat with channels (FA1 in Figs. 6 and 7) This facies association is composed of red and green mudstones, red fine-grained sandstones and metre-thick tabular sandstones. The mudstones are generally massive and arranged in metre-thick tabular strata, occasionally showing slickensides, mottling and traces of root bioturbation. The red fine-grained sandstones are centimetre- to decimetre-thick lenticular layers, occasionally with irregular bioturbated bases and vertical burrows. Sandstones display wave and current ripple cross-lamination, interference ripples, planar and through cross-bedding, herring-bone cross stratification, tool casts, mud drapes, slickensides, bivalve fragments, and *Arenicolites, Skolithos* and *Planolites* ichnofossils. The sandstones pinch out towards the north and south.

This facies association is interpreted as a tidal flat environment in which the background sedimentation of fine-grained particles settled from suspension under low-energy conditions. The centimetre- to decimetre-thick sandstones containing *Arenicolites* are interpreted as distal washover fan deposits interbedded with mudflat mudstones.

(C) Carbonate lagoon (FA2 in Figs. 6 and 7). This facies association is composed of carbonates and interbedded ochre- and white-coloured sandstones. The carbonates are limestones and marls containing bivalves, gastropods, charophytes and ostracods and, occasionally, benthic foraminifera, oysters, fish teeth, vertebrate bone fragments, dasycladacean, and plants. The facies associations are interpreted as representing the sedimentation in a carbonate lagoon. The sandstones contain charophytes, plant and bivalve fragments; they are fine-grained centimetre- to decimetre-thick tabular strata thinning northwards and southwards. They pinch out into the lagoonal sediments and exhibit sub-parallel and undulating lamination, cross-lamination, asymmetric ripple lamination and local deformation as slump and flame structures. The sandstones are interpreted as distal washover fan deposits that interrupted the background low-energy conditions conducive to carbonate sedimentation in the lagoon.

(D) Flood-tidal delta (FA3 in Figs. 6 and 7). This facies association appears as a fining-upwards sandy body, 6 m thick and 4 km long. In the study area, the facies pinches out in the southern sector of the profile within the carbonate lagoon facies. The sand body shows a generally lenticular geometry with a sharp and flat base (with tool casts and locally horizontal bioturbation), and a convex top. The facies association is interpreted as a flood-tidal delta comprising facies of both flood ramp and flood delta origin. These facies are vertically related, suggesting a flood-tidal delta encased in mixed carbonate lagoonal deposits.

(E) Barrier island–tidal inlet (b.i./inlet) (FA4 in Figs. 6 and 7). This facies association consists of a 6-m-thick lenticular body of very coarse- to fine-grained sandstone containing scattered

oysters shells, fish teeth, clay and quartzite pebble lags, vertebrate bones and metre-long tree trunks at the base. Internally, the sand body is divided by large-scale planar to slightly concave-up lateral accretion surfaces, inclined to the northeast and with aligned basal lags (clay, quartzite and minor bioclasts). The deposit is interpreted as a multistory body representing a barrier island system and associated inlet channels. The occurrence of a channel body showing large-scale accretion surfaces is interpreted as a tidal inlet encased in a barrier spit.

5. Study of the reservoir sandstones

According to the thickness and lateral continuity of sandstone bodies, the basal tsunami deposit and the uppermost barrier island/inlet deposit were selected for their study as reservoir analogues (Fig. 7). In these sandstone deposits, a high-resolution characterization of heterogeneities at different scales, and the relationship of these heterogeneities to porosity and permeability parameters have been carried out. Other facies associations located between tsunami and b.i./inlet deposits (Figs. 6 and 7), consisting of clay, marl and micritic carbonate lithofacies were not included in this study due to their lithology. The sandstone deposits of the FA1 (tidal mud flat with channels) and FA3 (flood-tidal delta) facies associations were also excluded from this study because they are laterally discontinuous and pinch out in the clay deposits within the study area at the Aliaga outcrop.

5.1. Sandstone deposits at the mesoscopic scale: facies analysis

The descriptions at the mesoscopic scale (decimetres to tens of meters) of the geometry of internal lithofacies and their distributions were obtained in 2D perspectives: horizontal in N-S direction and vertical (thickness). The lithofacies distinguished by Navarrete *et al.* (2013a, 2014) were used for mesoscopic scale facies mapping from drone photograph analysis and field observations.

5.1.1. Tsunami deposit

The tsunami deposit, located at the base of the Aliaga outcrop (Figs. 4, 6 and 7), consists of a multiple-bed deposit of sandstone and conglomerate of variable thickness (30–50 cm to 3–4 m It shows a flat-lying geometry with an irregular basal surface. The sedimentology and architecture of the track-bearing sandstone are based mainly on field observations made from 20 stratigraphic sections logged in detail, and interpretations from drone photographs. Sedimentological features, such as grain size and sedimentary structures, allowed the discrimination of four lithofacies (Navarrete *et al.*, 2014), with being three of them present at the sandstone body in the Aliaga outcrop (Fig. 8): a conglomerate facies (LF1), a ripple and megaripple facies (LF2) and an oscillation ripple facies (LF3).

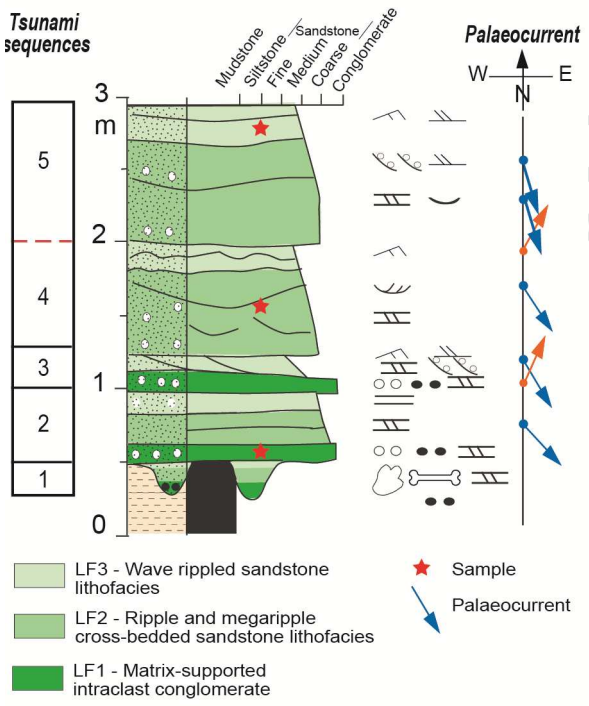

Fig. 8: Vertical sedimentary architecture of the tsunami deposit (modified from Navarrete *et al.* 2014).

Lithofacies LF1 is a conglomeratic facies with matrix-supported clasts of greenish, angular carbonate pebbles (with armoured external surface), and plant and dinosaur bone fragments in a whitish coarse-grained sandy matrix of feldspar and quartz grains along with minor

zircon, rutile, tourmaline, glauconite and apatite grains (Fig. 9A, B and C). This lithofacies is recognized mainly at the base of the deposit, as dinosaur track cast infill (Fig. 9A), where tracks are present. In other zones of the North sector, this facies is locally preserved in the middle of the bed, at the base of an intermediate sedimentary succession (Figs. 9B and 10). The LF1 lithofacies is generally massive, although it locally shows faint cross-laminations, horizontal laminations and fining upward (Fig. 9C). Cross-stratification planes measured in sedimentary sections 3 and 4 (Figs. 4 and 7) indicate a N–NNE palaeo-flow direction (Fig. 9C). The geometry of the LF1 lithofacies is usually lenticular, with a length of 1–10 m and thickness of 2–15 cm (Fig. 9B and D and Fig. 10). This lithofacies was only mapped in drone photographs where its thickness was >5 cm and its length >1–2 m.

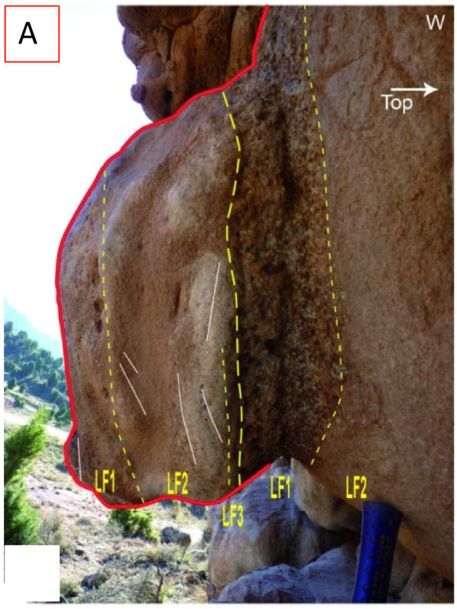

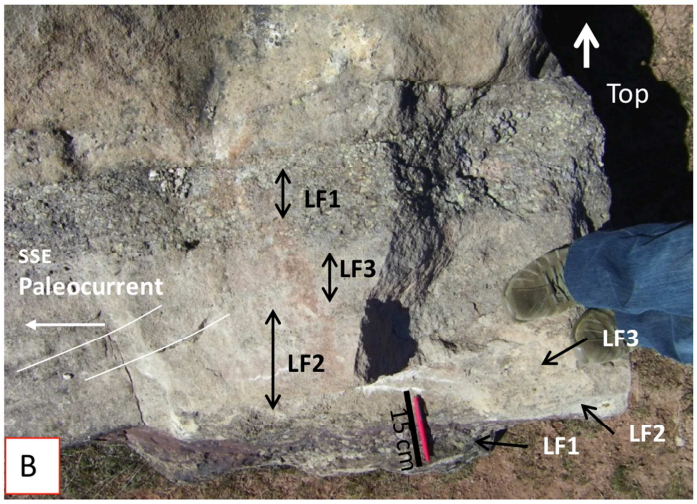

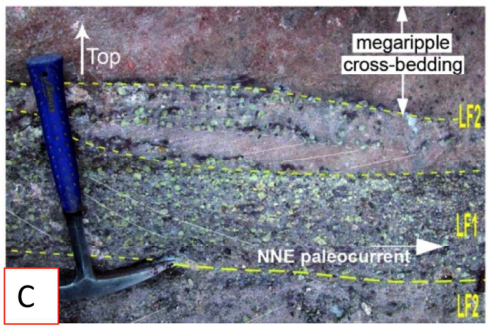

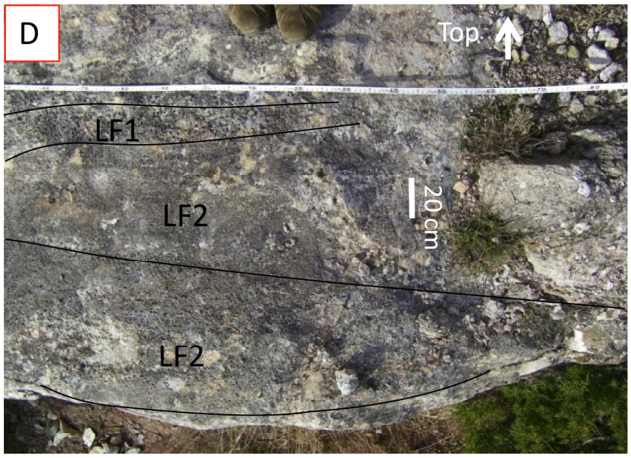

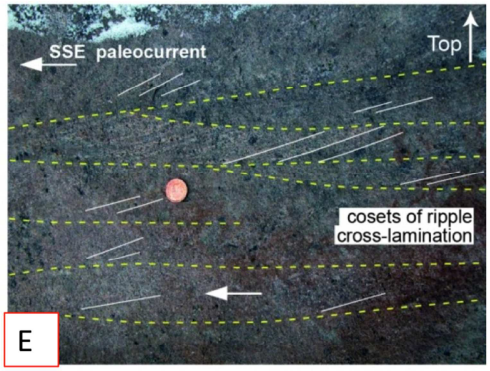

Fig. 9: Field view of tsunami lithofacies at section 2 (see location in Figs. 4 and 7). (A) The lithofacies LF1 occurs as dinosaur cast infill. (B) Field view of the sedimentary succession showing the lithofacies arrangement in the sedimentary succession. Palaeocurrent indicators in lithofacies LF2 indicate flow towards the SSE. (C) Lithofacies LF1 with cross-stratification indicating a palaeocurrent direction towards the NNE. (D) Detail showing lithofacies LF1 and LF2. (E) Detail of lithofacies LF2 showing a fining upward sequence with cm-scale planar cross-stratification (palaeocurrent towards the SSE).

According to Navarrete *et al.* (2014), the nature of the LF1 lithofacies suggests transport by powerful currents during an upper flow regime (Bondevik et al., 1997), with rapid deposition (Sugawara et al., 2008) and mixing of sediment from different sources. The occurrence of floating armoured carbonate pebbles indicates that they were transported, and finally deposited in a clear traction carpet of a high-density current (e.g., Lowe, 1982; Sohn, 1997). The faint lamination also suggests deposition from upper flow regime conditions, where a gradual decrease of energy led to fining upward cycles.

The ripple and megaripple lithofacies (LF2) is the most abundant facies in the both sectors of outcrop (Figs. 8 and 10). It is composed of fine- to coarse-grained feldspar and quartz sand with fining-upward grain-size sequences and centimetre- to decimetre-scale sets of trough and planar cross-bedding (Fig. 9E); its geometry is wedge-shaped, with a thickness of 15–160 cm (Figs. 9D and 10).

The overall presence of planar and trough cross-bedding indicates that the flow organized the sand bed load (low-energy flow regime) into straight and sinuous crest megaripples, respectively. The vertical succession of LF2 to the underlying LF1 lithofacies, and the finer grain-size of LF2 with respect to LF1 suggest their deposition from a flow with continuous decaying of its energy (Navarrete *et al.*, 2014).

Lithofacies LF3 is scarce and is composed of fine- to medium-grained feldspar and quartz sand with an upward decrease in grain size, with mud drapes and mud layers; its thickness at the Aliaga outcrop is 5–28 cm and its contact with LF2 is gradual (Figs. 8 and 9B). This facies shows asymmetrical climbing ripples and cross- and parallel laminations.

The finer grain-size of LF3 indicates sedimentation from a lower-energy flow. The presence of asymmetric climbing ripples, mud drapes and mud layers is interpreted as representing deposition during the waning period at the last stage of a flood event (Fujiwara, 2008).

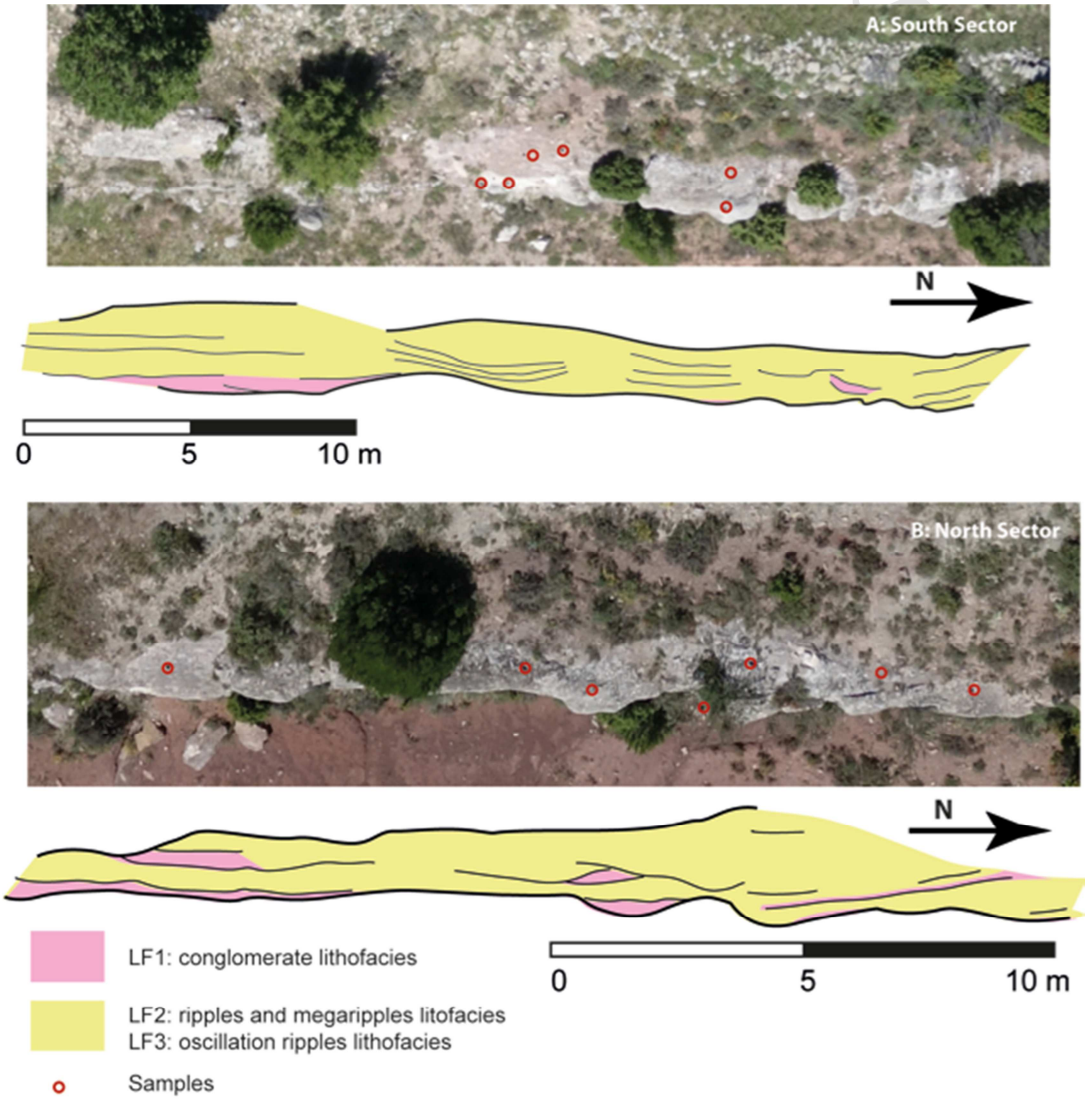

Fig. 10: Tsunami deposit in drone photographs and lithofacies maps at mesoscopic (outcrop) scale (lithofacies as those described by Navarrete *et al.*, 2014). (A) Profile of the South sector. (B) Profile of the North sector.

According to Navarrete et al. (2014), tsunami deposition took place by settling from a hyperconcentrated flow. Each fining upward sequence reflects likely deposition from a wave, and its progressive waning. In overall, it represents a catastrophic sedimentary event with at least five episodes of inflow and backflow of wave trains (Fig. 8), related to sediment deposition and reworking, respectively (Navarrete *et al.*, 2014). Based on regional palaeogeographical data, these authors have interpreted that the NNE-directed palaeocurrents recorded in the tsunami deposit represented inflows from open marine areas towards the lagoon, and those SSE-directed backflows controlled by antecedent topography.

A preliminary map of these facies was drawn on a drone photograph to delimit the geometry of the lithofacies deposit at the mesoscopic (outcrop) scale (Fig. 10). Lithofacies LF2 and LF3 are similar in colour and were difficult to distinguish on the drone photographs.

5.1.2. Barrier island / inlet deposit

The barrier island - tidal inlet (b.i./inlet) deposit is located at the top of the outcrop profile (Figs. 4, 6 and 7) and was described in detail by Navarrete et al. (2013a). This deposit comprises a 6-m-thick lenticular body of ochre-coloured very coarse- to fine-grained sandstone with scattered oysters shells, fish teeth, pebbles, and clay and quartzite pebble lags. The base of the sandstone body shows oriented tree trunks m-long and vertebrate bone fragments, *Planolites* and *Thalassinoides* and tool casts. Internally, the sandy body is divided by large-scale planar to slightly concave-up lateral accretion surfaces, inclined to the NE and aligned with basal lags (clay, quartzite and minor bioclasts). The accretion surfaces separate

dm- to m-thick inclined strata internally arranged in cm-thick trough and planar cross-bedded sets (Fig. 11A, 11B, 11C). This sandy body also shows parallel lamination, drapes, carbonaceous plant fragments (Fig. 11D) and, locally, asymmetric wave ripples on top of the cross-bedded sets. The palaeocurrent is towards the SE and ESE and, occasionally, towards the NE and ENE and, locally, an E–W bipolarity has been also observed in minor structures.

Based on the decribed feactures, Navarrete et al. (2013a) interpreted this deposit as a multistory body constituting a barrier island system (Kumar and Sanders, 1974; Donselaar, 1996), the main SE to ESE unidirectional flow representing the flood inside the barrier island, and the inclined major surfaces towards the NE representing the tidal inlet accretion surfaces moved by the main longshore drift current. In such a context, NE and ENE palaeocurrents would represent the flood palaeocurrent dispersion and E–W bipolarity in minor structures the flood and ebb. Variations in flow energy, probably associated with tidal flows, was suggested by Navarrete et al. (2013a) from the existence of drapes with carbonaceous plant fragments and asymmetric wave ripples within the deposit .

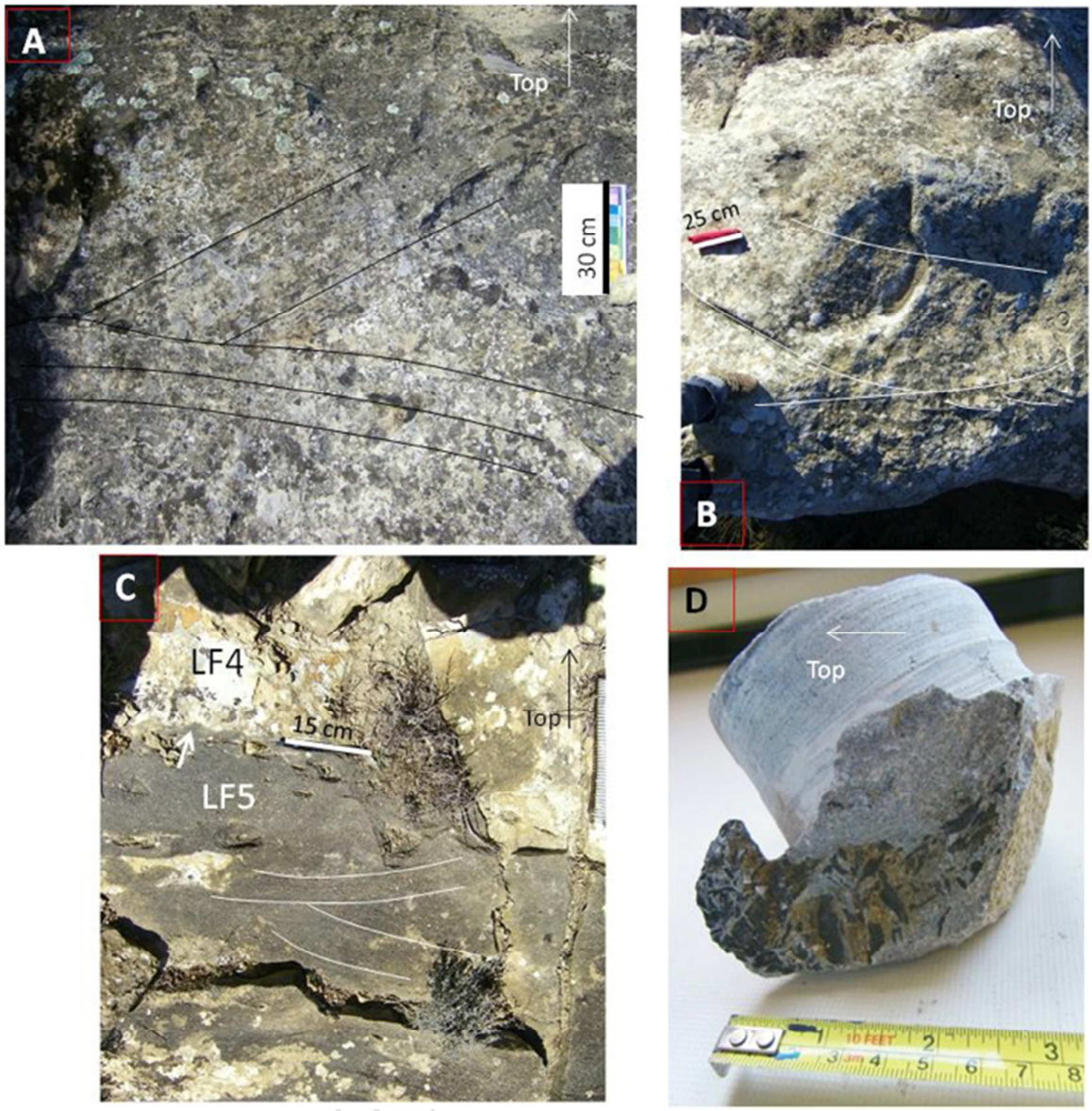

Fig. 11: Field view of the barrier island (b.i.)/inlet facies. (A) and (B) Lithofacies LF4 in the South sector outcrop showing decimetre-thick trough cross-bedding and planar cross-bedding sets. (C) Lithofacies LF4 and LF5 in the North sector outcrop showing centimetre-thick trough cross-laminations and asymmetric wave (arrow) structures. (D) Plant fragments accumulation in sample 59.

A detail outcrop study of this deposit has allowed the identification of two different lithofacies, referred here as LF4 and LF5. The lihofacies LF4 is an ochre-coloured medium- to fine-grained sandstone with decimetre-thick trough cross-bedding sets (maximum thickness,

35 cm) and centimetre-thick planar cross-bedding sets (maximum thickness, 8 cm). The basal surface is slightly concave and includes metre-long tree trunks and vertebrate bone fragments; the top surface is flat (Fig. 7). This lithofacies was generated by the migration of minor megaripples that were moved by flood and ebb water fluxes under low-energy flow regimes in the shoreface zone of a tidal inlet/barrier spit (Navarrete *et al.*, 2013a). Lithofacies LF5 is a grey very-fine-grained cemented sandstone with centimetre-thick trough cross-lamination sets, drapes, locally interfering ripple crests and asymmetric wave ripples on top of the cross-bed sets (Fig. 11**Error! Reference source not found.**C), scattered oysters, fishes teeth, and centimetre-thick accumulations of bioclast or carbonaceous plant fragments (Fig. 11D). LF5 was probably associated with tidal flows between brackish and marine subenvironments (Navarrete *et al.* 2013a).

At the outcrop scale, the b.i./inlet deposit shows a heterogeneous lithofacies distribution and different thickness between the North and South sectors (Fig. 12). In the South sector, the deposit is 3–7 m thick and lithofacies LF4 is dominant (12A). In the North sector, the deposit is thinner (1–3 m) but the two facies (LF4 and LF5) are present (Fig. B). This change in thickness and facies between both sectors is probably related to a variation of the sedimentary environment. These variations will be discussed in section 6.

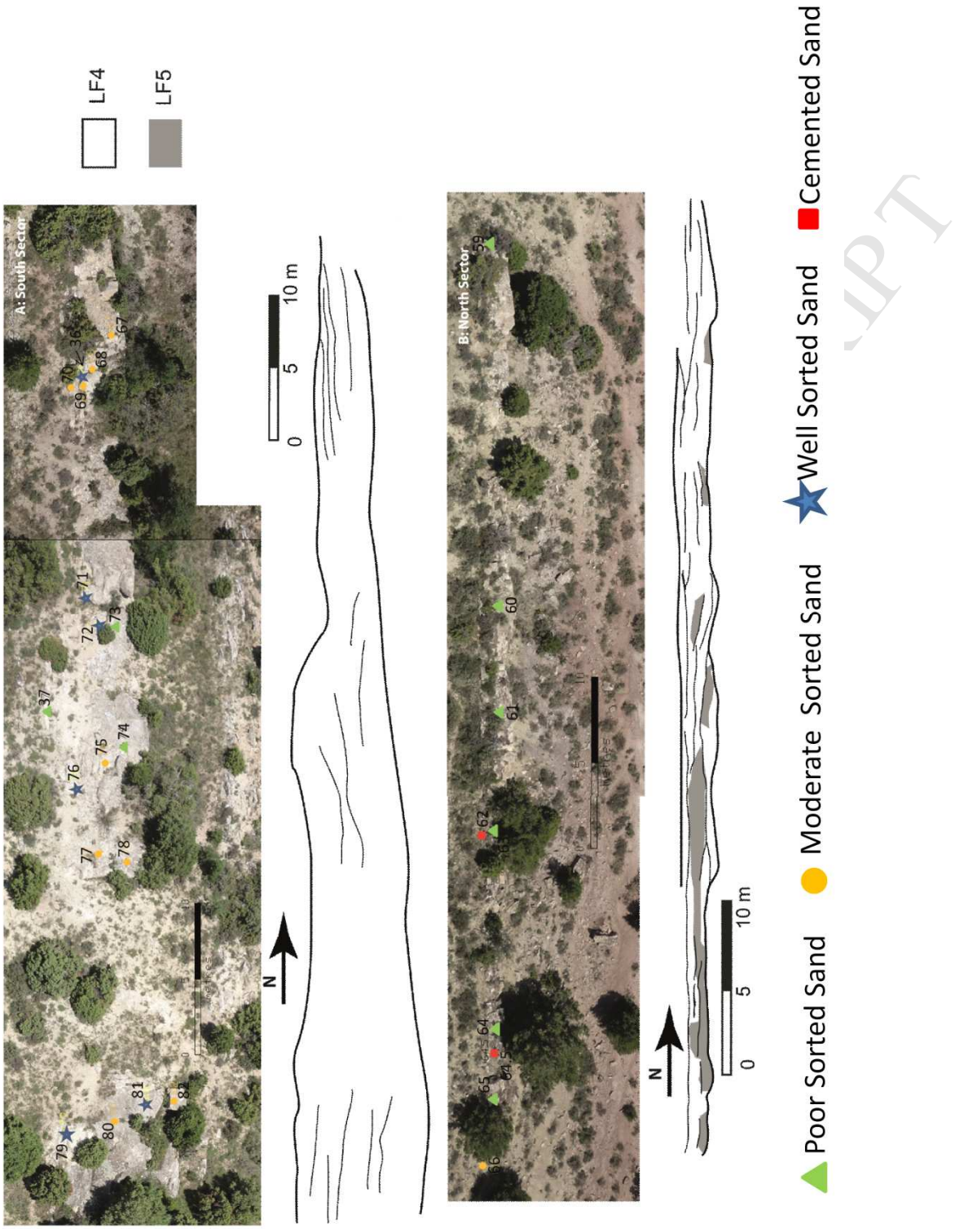

Fig. 12: Drone photographs of the barrier island/inlet deposit. A) South sector profile. B) North sector profile.

5.2. Sandstone deposits at the microscopic scale: petrological characterization

Based on analyses of 65 thin sections, the petrological characterization of the previously described lithofacies is carried out in this subsection. This includes the estimates of the grain-size distribution and the sand sorting of the sandstone facies, as well as of their bulk composition.

A preliminary analysis of samples of tsunami and b.i./inlet deposits showed that nearly every sample was an arkosic or subarkosic sandstone, with an average composition of 10% clay matrix, 60% quartz (monocrystalline and a few polycrystalline samples), 20% feldspar (plagioclase and K-feldspar) and 10% lithic fragments. This mineralogical homogeneity excluded a mineralogical classification of the lithofacies, and thus the lithofacies were classified as a function of grain size distribution, sand sorting, and cement content.

5.2.1. Microfacies of the tsunami deposit

The petrological characterization of the tsunami lithofacies was based on analyses of 36 thin sections. The locations of these samples along the outcrop are shown in Fig. 13. All samples are subarkosic–arkosic sandstones, containing 10% clay matrix, 50%–70% quartz, 10%–20% feldspar and 5%–15% lithic fragments with mud clasts and micas as the main lithic grains (see detail in table 1). Kaolin and calcite are the most common cements; their contents vary from trace amounts to 10% (Fig. A); a few samples contain trace amounts of dolomite cement (Fig. D). The main accessory minerals are tourmaline and trace amounts of phosphate and organic matter. Sedimentary structures, where present, consist of trough cross-bedding with an apparent direction to North. The upward decrease in grain size is apparent at the microscale, and some samples exhibit bimodal grain-size distribution (Fig. C). Fractured quartz and feldspar grains are abundant in many samples (Fig. A and B). The red colour of the sandstone in the southernmost part of the South sector profile is probably related to the relatively high K-feldspar content (sample 83, Fig 13A and Fig. B).

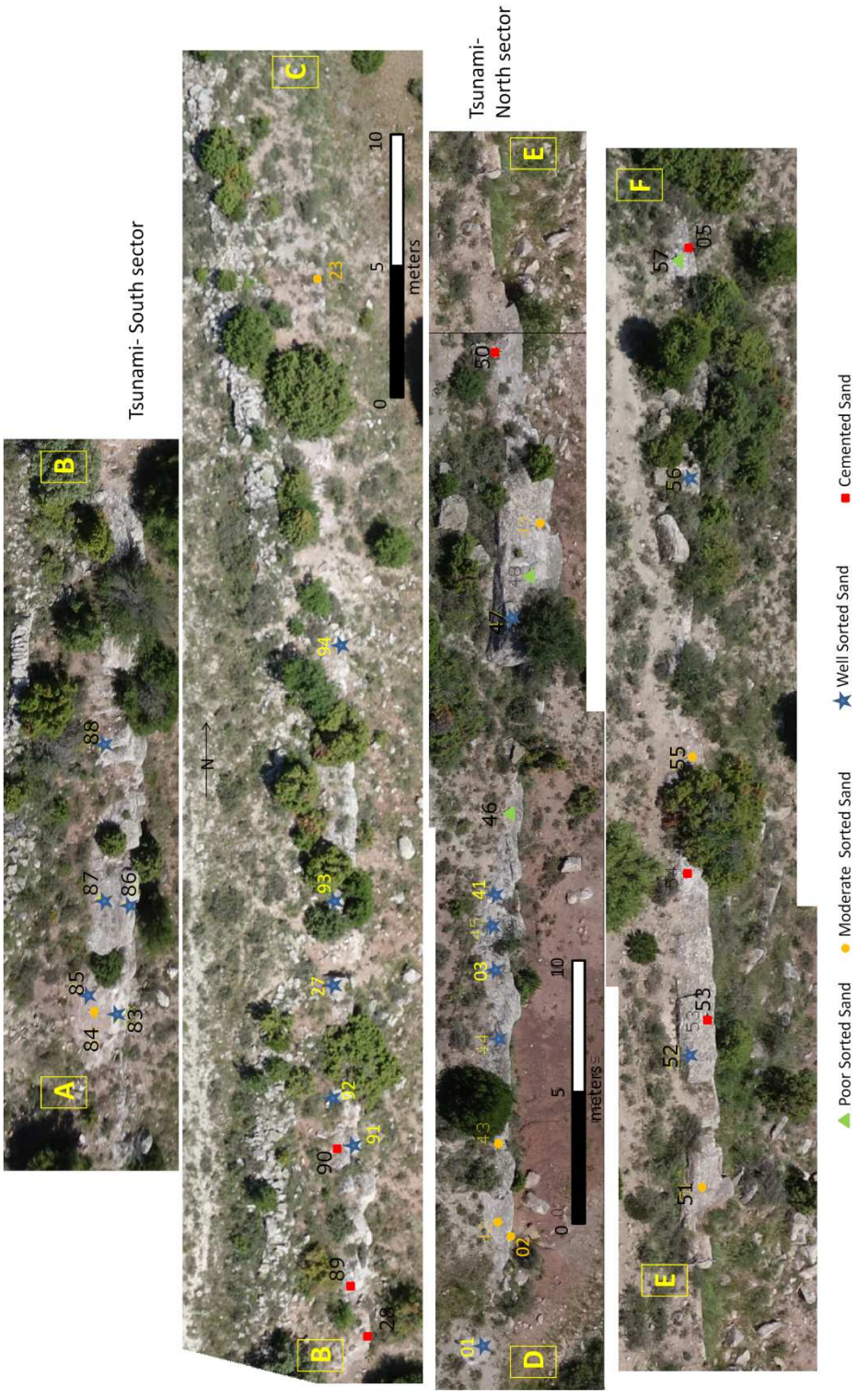

Fig. 13: Drone photographs showing the spatial distribution of collection localities of tsunami samples, classified according to the degree of sorting and cementation (see legend). The photographs extend from the South (upper photograph) to the North (lower photograph) sector. The letters 'A', 'B', etc., indicate points of photo joint, which were plotted in the Fig.4.

Table 1: Tsunami deposit samples and their petrographic and petrophysical characteristics. Table headings: Phi is measured porosity; Kh and Kv is measured horizontal and vertical permeability respectively; % Clast is the sum of quartz, feldspar and lithic grains; % Cement is the amount of cement content which can be calcite, kaolin and dolomite; Sorting is the sand sorting at microscopic scale; Grain Size is the average sand size at microscopic scale; Facies is the code to distinguish sorting facies class; and Profile sector is the location of sample in the outcrop face.

Sample	Phi (m^3/m^3)	Kh (mD)	Kv (mD)	% Clast (Qtz+F+L)	% Cement	Sorting	Grain Size	Profile sector
1				80		well	medium	North
2				80	3	Moderate (bi-modal)	fine-coarse	
3				80	3	well	fine-medium	
5				50	50	moderate	medium-coarse	
41	0.197	13.9	14	65	7	well	fine-medium	
42	0.0663	0.17		65	7	moderate	medium-coarse	
43	0.076	2.1		70	5	moderate	medium-coarse	
44	0.1676	7.91		85		well	medium	
45	0.1859	10.3		85		well	fine-medium	
46	0.1272			85	3	poor	coarse-very coarse	
47	0.1795	7.84		85	3	well	medium	
48	0.1685	10.45		70	7	poor	fine-medium	
49	0.1846	14.24	10.89	85	3	moderate	fine-medium	
50	0.1714	5.15	4.57	70	10	well	fine-medium	
51	0.1647	4.83		80	3	moderate	medium-coarse	
52	0.1769	6.55		80	3	well	fine-medium	
53	0.173	7.77	7.73	65	10	poor	fine-coarse	
54	0.1437	5.17		65	10	poor	medium-coarse	
55	0.1893	8.09	7.7	70	7	moderate	medium-coarse	
56	0.1847	7.47		75	3	well	fine-medium	
57	0.1796	6.5		75	3	poor	fine-coarse	
23				70	10	moderate	medium-coarse	South
27				80	5	well	fine	
28	0.111	1.57	1.96	65	10	well	fine	
83	0.1874	14.96		80	5	well	medium	

Sample	Phi (m^3/m^3)	Kh (mD)	Kv (mD)	% Clast (Qtz+F+L)	% Cement	Sorting	Grain Size	Profile sector
84	0.2041	26.65	20.89	70	5	moderate	medium	
85	0.1663	5.91	7.02	85	5	well	medium	
86	0.2131	28.76	24.09	75	7	well	medium-coarse	
87	0.1962	11.04		75	10	well	fine-medium	
88	0.1879	10.19	11.14	75	7	well	fine-medium	
89	0.1637	8.29	21.21	70	10	well	fine-medium	
90	0.171	9.25	9.06	70	10	well	fine-medium	
91	0.1565	5.48		80	7	well	fine-medium	
92	0.1684	8.14		75	10	well	fine	
93	0.1763	6.99		75	7	well	fine	
94	0.1437	2.99		75	7	well	fine-medium	

The samples were first classified as a function of sorting and cementation (Table 2); three sorting facies and a cemented facies were defined: (0) poorly sorted sandstone (PSs facies), (1) moderately sorted sandstone (MSs facies), (2) well-sorted sandstone (WSs facies) and (3) cemented sandstone (CSs facies). Samples with bimodal grain-size distribution were classified as MSs facies, and those with a cement content > 10% as CSs facies. The Table 2 summarizes the number of samples by sorting class and the equivalent lithofacies at the mesoscopic scale. Half of the samples were classified as WSs facies. Almost every sample was classified as WSs facies in the South sector (Fig. 13 and Table 2), and in the North sector the MSs and WSs are the most important facies (Fig. 13 and Table 2). The cemented samples were found in both sectors at different locations: at the base, middle and top of the profile. The cemented samples are also classified as function of sorting and comprised the Wss and Pss facies. The dinosaur footprints were sampled infrequently, and are generally filled with PSs facies.

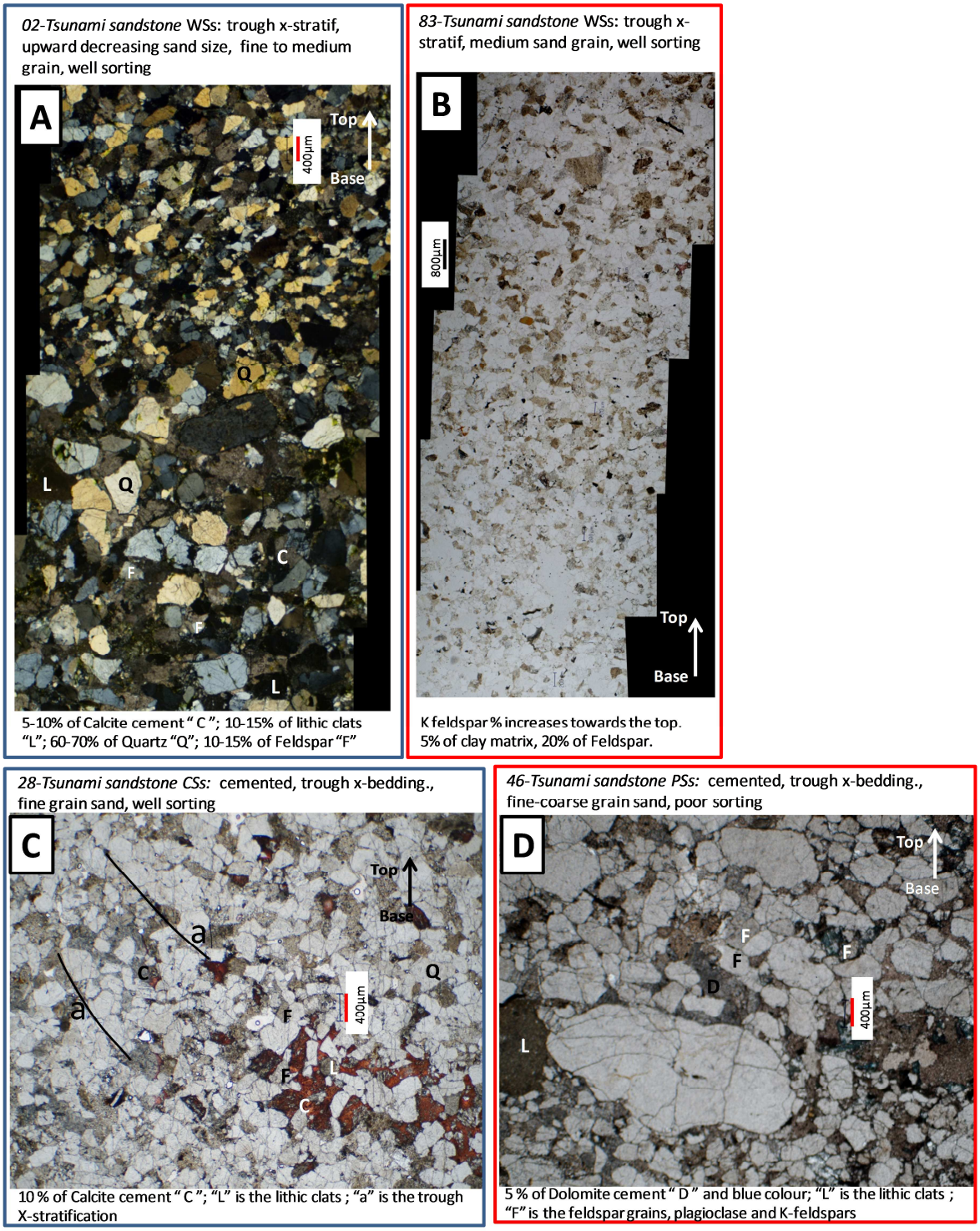

Fig. 14: Thin sections of tsunami deposit samples. (A) Sample no. 2: WSs facies showing upward-decreasing sand size from medium to fine sand. Cross polarized light. (B) Sample no. 83: WSs facies showing a medium sand size, with the K-feldspar content increasing towards the top of the sample. Plane polarized light. (C) Sample no. 28: Css facies showing a fine sand size and good sorting. Plane polarized

light. (D) Sample no. 4: Pss facies showing traces of dolomite cement and fractured quartz. Plane polarized light

Table 2: Tsunami deposit facies classes based on degree of sorting and cement content and equivalent lithofacies. Table variables: Name is the abbreviation of facies classification by sorting; Lithofacies mesoscopic scale is the equivalent facies described by Navarrete *et al.* (2014); North and South are the quantity of samples in each sector; and Total is the sum of samples by facies.

	Tsunami sandstone			
Name	Lithofacies mesoscopic scale	Samples		
		North	South	Total
PSs	LF1	3	0	*3*
MSs	LF2	6	2	*8*
WSs	LF2 or LF3	8	10	*18*
CSs	LF1 or LF2	4	3	*7*
Total		21	15	*36*

Samples were also classified as a function of grain size distribution following Folk (1980). They were grouped into five grain-size facies classes: coarse grained, medium–coarse grained, medium grained, fine–medium grained and fine grained (Table 3). The equivalent grain-size facies classes and mesoscopic scale lithofacies are listed in Table 3. Half of the samples were classified as fine- and fine- to medium-grained sand and other 40% as medium and medium-coarse grained; four samples were classified as coarse-grained sand and are located in the North sector.

Table 3: Tsunami classification based on grain size and equivalent sorting facies class and mesoscopic scale lithofacies. 'Sorting class' for a given class are listed in order of abundance.

	Number of samples				
Class	North	South	Total	Sorting class	Lithofacies mesoscopic scale
Coarse	4	0	4	PSs	LF1
Medium-coarse	6	2	8	MSs,WSs, PSs	LF2

Medium	3	3	6	Wss, MSs	LF2
Fine-medium	8	6	14	WSs,MSs,Pss	LF2
Fine	0	4	4	WSs	LF3
Total	21	15	36		

The tsunami deposit facies is relatively homogeneous when classified in terms of sorting, with 70% of the facies classified as WSs and MSs facies. In terms of grain size, samples are spread into fine- to coarse-grained, with an abundance of fine- to medium-grained. Generally, the fine-grained sands are well sorted (WSs) or moderate sorted (MSs) facies, and the coarse-grained sands are poorly sorted (Pss; Table 3). The lithofacies at the mesoscopic scale are strongly correlated with grain-size facies classes than sorting facies classes. However, samples classified as function of sorting show a clearly heterogeneity in facies distribution independently of the grain-size distribution (Table 1): in the South sector, the WSs facies is dominant, while in the North sector, all facies are present.

5.2.2. Microfacies of the b.i./inlet deposit

The petrological characterization of the b.i./inlet lithofacies was based on observations of 30 thin sections (Table 4). The location of the samples in the outcrop is shown in Fig. . All samples are subarkosic–arkosic sandstones consisting of 5%–15% clay matrix, 50%–70% quartz, 10%–20% feldspars, and 10%–25% lithic fragments dominated by mud clasts and bioclasts. Tourmaline is the most abundant accessory mineral, followed by opaque minerals and phosphate. Sedimentary structures, when present, are trough cross-bedding with apparent N–S orientations. The sands have a bimodal grain-size distribution (Fig. 15A). Fractured quartz grains are less numerous than in the tsunami deposit, and authigenic kaolinite is locally present (Fig. 15B). The cement is principally dolomite and locally calcite or kaolin (Fig. 15C), and it generally makes up less than 10% of the whole rock (Table 4), except

in some samples in the North sector from the LF5 lithofacies, where the matrix has been entirely replaced by dolomite cement (Fig. 15D).

Table 4: B.i./inlet samples and their petrographic and petrophysical characteristics. Table headings: Phi is measured porosity; Kh and Kv is measured horizontal and vertical permeability respectively; % Clast is the sum of quartz, feldspar and lithics grains; % Cement is the amount of cement content which can be calcite, kaolin and dolomite; Sorting is the sand sorting at microscopic scale; Grain Size is the average sand size at microscopic scale; Facies is the code to distinguish sorting facies class; and Profile sector is the location of sample in the outcrop face.

Sample	Phi (m^3/m^3)	Kh (mD)	Kv (mD)	% Clast (Qtz+F+L)	% Cement	Sorting	Grain Size	Profile sector
18				70	5	moderate	Fine-medium	North
19				70	10	moderate	fine	
20				70	10	moderate	fine_medium	
39	0.115	0.9	0.5	60	5	poor	medium	
60	0.1545	8.24	9.58	70	7	poor	coarse	
61	0.165	14.42		75	3	poor	medium-coarse	
62	0.0236	0.01		50	40	moderate	medium	
63	0.1489	4.28	2.85	65	7	poor	medium-coarse	
64	0.1492	3.53		75	3	poor	medium-coarse	
64.5	0.0239	0.02		50	30	poor	fine-medium	
65	0.064	0.09		70	7	poor	medium-coarse	
66	0.1127	0.7		75	3	moderate	medium-coarse	
36	0.21	16	16.5	90	3	well	fine-medium	South
37	0.14	2	4.2	70	5	poor	fine-medium	
67	0.1947	8.87		85	3	moderate	medium-coarse	
68	0.2028	11.23		70	5	moderate	medium-coarse	
69	0.1804	9.6		75	5	moderate	medium-coarse	
70	0.1516	6.79		85		moderate	fine-medium	
71	0.1945	15.33	12.14	80	7	well	medium	

72	0.1803	9.25	14.2	80	5	well	medium	
73	0.1793	6.79		85	5	poor	fine-medium	
74	0.1871	6.64	7.38	80	5	poor	fine-medium	
75	0.2086	11.9		90	3	moderate	medium-coarse	
76	0.1842	7.59		75	3	well	fine-medium	
77	0.1886	8.25		80	5	moderate	coarse	
78	0.1864	9.08	8.3	75	7	moderate	medium-coarse	
79	0.1778	8.1	8.51	75	5	well	fine-medium	
80	0.1135	2.03		70	7	moderate	medium-coarse	
81	0.2175	12.89	14.63	80	3	well	fine-medium	
82	0.1279	5.72		70	7	moderate	medium-coarse	

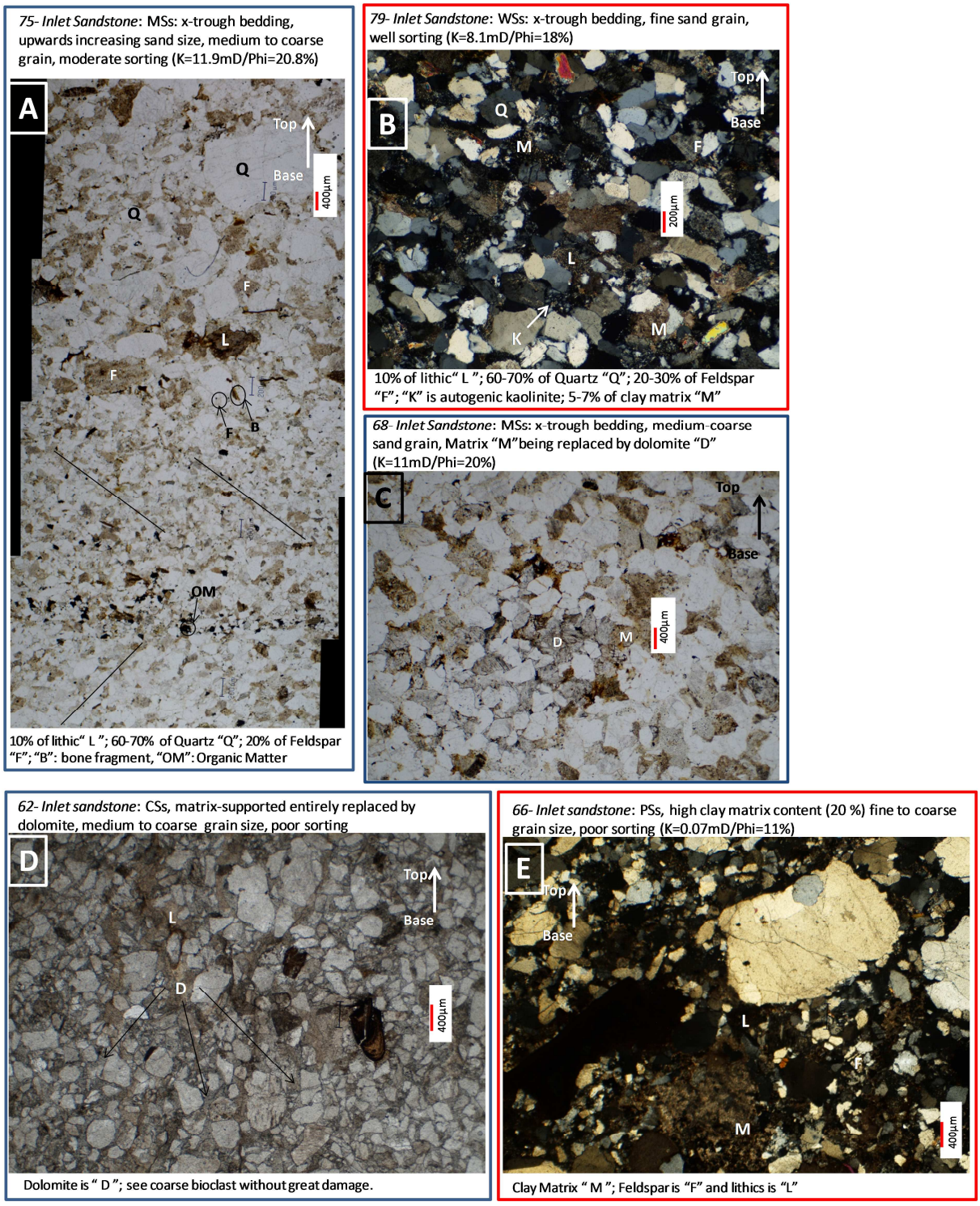

Fig. 15: Photomicrographs of b.i./inlet deposit sandstone samples. (A) Sample no. 75 (South sector): MSs facies showing apparent bi-directional palaeocurrent directions. Plane polarized light. (B) Sample no. 79 (South sector): WSs facies showing fine sand and authigenic kaolinite. Cross polarized light. (C) Sample no. 68 (South sector) from the MSs facies showing clay matrix replaced by dolomite. Plane polarized light. (D) Sample no. 62 (North sector) from the CSs facies with matrix entirely replaced by dolomite.

Plane polarized light. (E) Sample no. 66 (North sector) from the PSs facies showing very coarse grain sizes. Cross polarized light.

Based on the classification used in Section 5.2.1, samples were classified by the degree of sorting and cemented content into the PSs, MSs, WSs and CSs facies (Table 5). Samples with bimodal grain-size distribution were classified as MSs facies, and cement samples were considered as those with a cement content that made up >10% of the total rock. The spatial distribution of samples classified by sorting facies class is heterogeneous in the deposit (Fig. 12 and Table 5); nearly all samples classified as WSs and MSs are located in the South sector, whereas most samples in the North sector were classified as PSs sorting facies class (Table 5 and Fig. 12). The CSs facies is only present in the North sector (Table 4, Fig. 12); CSs facies samples are also classified as function of sorting and are MSs and PSs facies.

Samples were also classified by grain-size facies class following the classification outlined in Section 5.2.1. The spatial distribution of samples classified in different grain-size classes shows that samples of the fine–medium facies class occur in the South sector profile (Table 6), whereas those from other grain-size facies classes are regularly distributed throughout the deposit (Table 6). Generally, samples of fine–medium and medium grain-size facies classes are also classified as WSs and MSs sorting facies classes, and samples of coarse or medium–coarse grain-size classes are also classified as PSs sorting facies (Table 6).

Table 5: B.i./inlet sorting facies classes and equivalent lithofacies

B.I/Inlet			
Lithofacies macro-scale	**Name**	**North**	**South**
LF4 or LF5	PSs	6	3
LF4 or LF5	MSs	2	9
LF4	CSs	4	0
LF4	WSs	0	6
		12	18

Table 6: B.i./Inlet grain-size facies classes and equivalent sorting facies classes and mesoscopic-scale lithofacies.

	Numbers of sample				
Class	**North**	**South**	**Total**	**Sorting class**	**Lithofacies mesoscopic scale**
Coarse	1	1	2	PSs, MSs	LF4
Medium-coarse	5	7	12	MSs, PSs	LF4
Medium	2	2	4	WSs, MSs, PSs	LF4 or LF5
Fine-medium	3	8	9	WSs, PSs, MSs	LF4 or LF5
Fine	1	0	0	MSs	LF5
Total	9	18	27		

The heterogeneity of the sandy facies distribution is more apparent when samples are classified by sorting and cemented facies rather than grain-size facies. A clear difference between the North and South sectors is observed in the abundances of the WSs and MSs facies in the South sector, whereas the PSs and CSs facies are abundant in the North sector. Samples classified by grain-size facies class show a homogeneous distribution in the deposit, except those of the fine–medium grain-size class, which are more abundant in the South sector.

5.3. Petrophysics

Fifty-six measurements of porosity (Phi) and horizontal permeability (Kh), and 23 of vertical permeability (Kv) were estimated from plugs. All plug samples were also classified by sorting

facies class and grain-size facies class (Tables 1 and 4). For all samples (from deposits in both Sectors), the range of porosity (Phi) values was 2%–22% and the permeability values were 0.01–28 mD. A plot of Phi versus Kh for all samples (Fig. 16) shows a strong correlation (correlation coefficient, r2, of 0.8 and 0.9 for the regressions of the tsunami and b.i./inlet deposits, respectively). In both deposits, Kv is strongly correlated with Kh (r2 = 0.85) (Fig.17); therefore, the permeability is considered to be isotropic, and no further analyses of Kv were performed in this study. The Phi and Kh values of the tsunami lithofacies are usually >14% and 3 mD, respectively, whereas the Phi and Kh values of the b.i./inlet deposit vary widely.

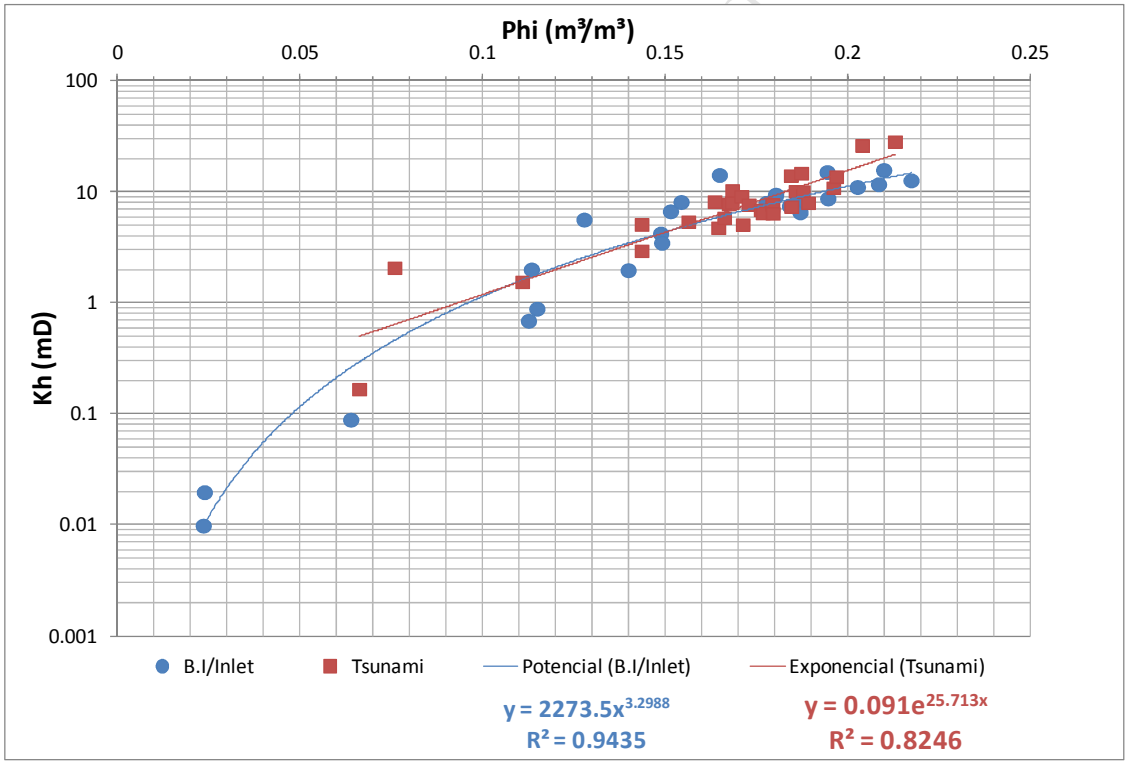

Fig. 16: Phi *versus* Kh for all samples. Red squares, tsunami deposit samples; blue circles, b.i./inlet deposit samples.

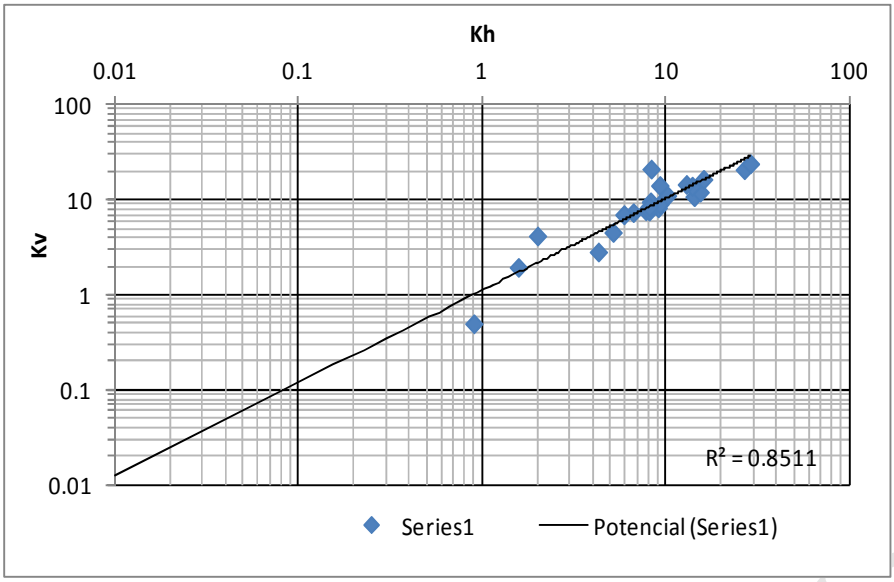

Fig. 17: Horizontal permeability (Kh) *versus* vertical permeability (Kv) for all samples.

5.3.1. Petrophysics of the tsunami deposit

The porosity (Phi) and horizontal permeability (Kh) of tsunami samples were measured on 30 plugs; the vertical permeability (Kv) was measured on 12 of these plugs. Samples were also classified as a function of sorting facies class and grain-size facies class (Table 1**Error! Reference source not found.**). The Phi versus Kh plot of tsunami deposit samples shows porosity varying from 14% to 22% and permeability from 3 to 22 mD (as outlined by the ellipse in Fig. 18A). This plot displays the samples according to their sorting facies class, and cemented samples were distinguished according to their sand sorting (shape of cemented point in Fig. 18). The values of Phi and Kh in North sector samples are lower for the MSs facies than for those in the South sector; values of Phi and Kh for samples of the PSs facies class lie within the ellipse shown in Fig. 18.

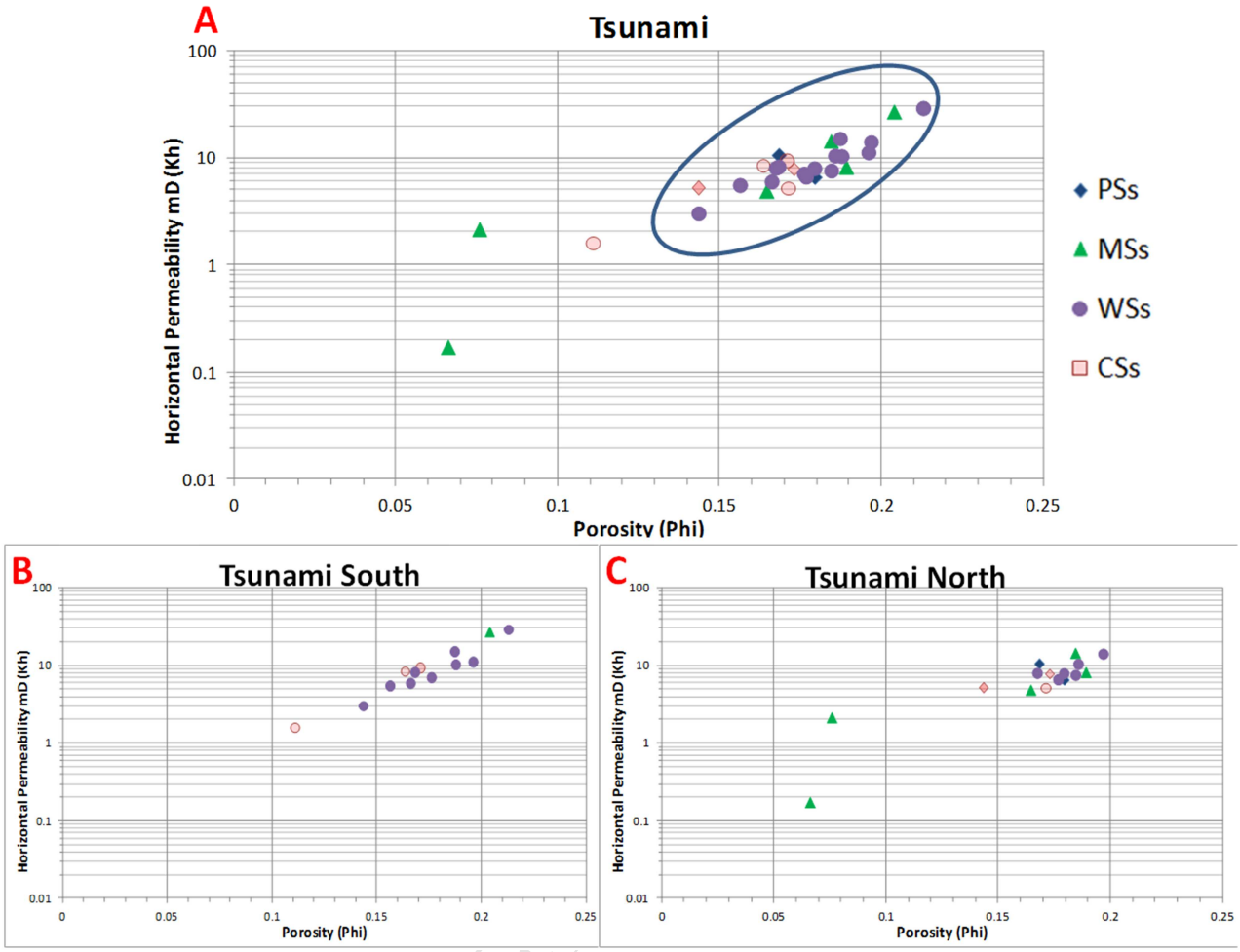

Fig. 18: Phi versus Kh plot for the tsunami samples, classified by sorting facies. Except for three samples, the porosity values lie in the range 0.14–0.22 (blue ellipse). The cemented samples (CSs class) are shown by pale red symbols with the point shape representing the sub-classification of sample, which is according to their sand sorting. (A) All samples. (B) Samples located at the South sector. (C) Samples located at the North sector.

Figure 19 shows the same Phi vs. Kh plot but samples are now distinguished according to their grain-size facies class. The three samples that fall outside of the ellipse in Fig. 19 belong to the medium–coarse grain-size class; one sample belonging to the fine grain-size class is also classified as the CSs sorting class. In the South sector (Fig. 19B), samples are principally

classified in the fine-medium grain-size class. In the North sector (Fig. 19C), half of the samples are classified in the medium-coarse grain-size class.

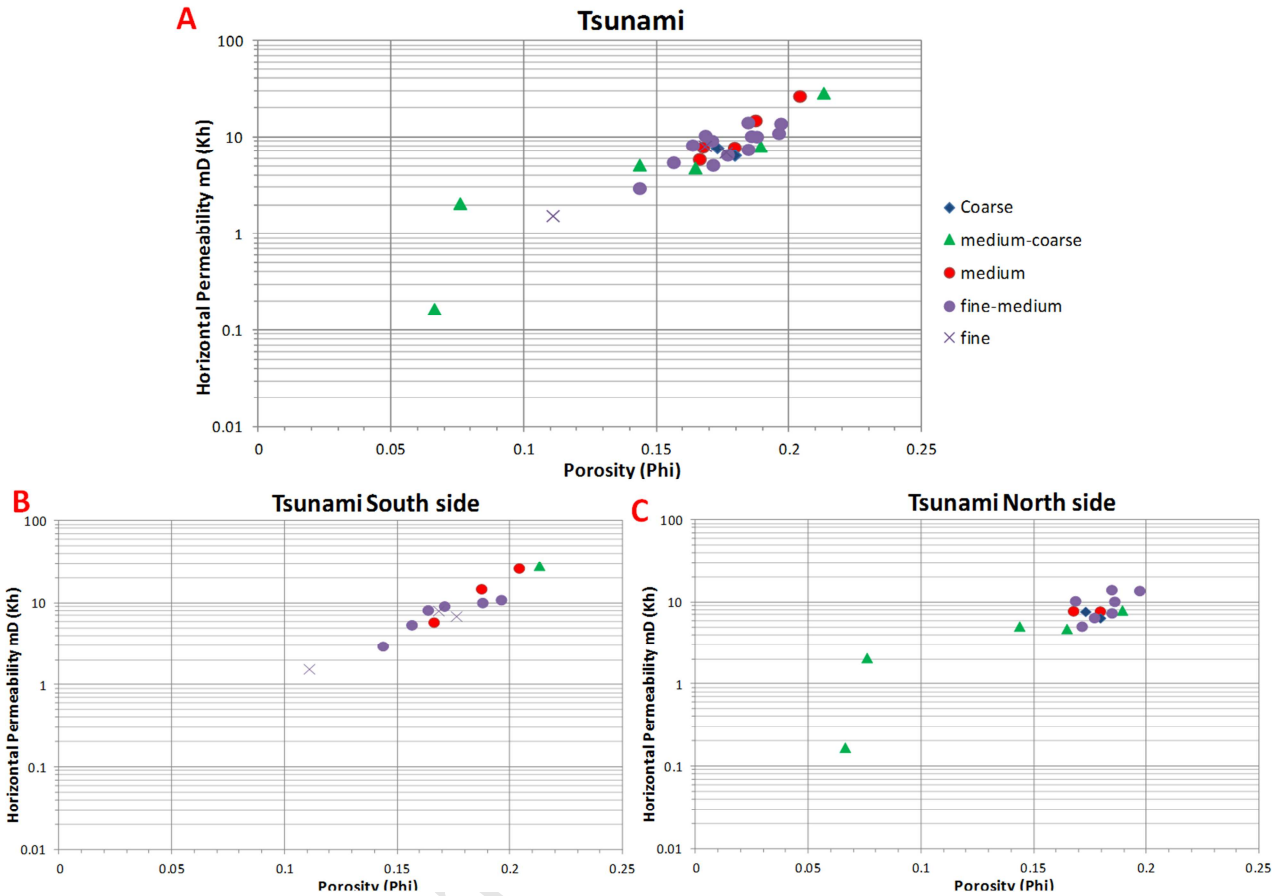

Fig. 19: Phi versus Kh plot for tsunami lithofacies, classified by grain-size facies class. (A) All samples. (B) Samples located at the South sector. (C) Samples located at the North sector.

The sorting and grain-size classes are relatively well correlated; generally, finer grain-size classes correspond to the WSs and MSs sorting facies classes, and the coarser grain-size classes correspond to the PSs and MSs facies classes (Table 3). Both classifications show a little difference in facies distribution between the North and South sectors.

5.3.2. Petrophysics of b.i./inlet deposit samples

The porosity (Phi) and horizontal permeability (Kh) of b.i./inlet samples were measured on 26 plugs (Fig. 20); the vertical permeability (Kv) was measured on 11 of these plugs (Table 4). Results are plotted in a Phi vs. Kh plot all together and also separately for each sector profile in Fig. 20. In the South sector (Fig. 20), permeability values are >1 mD and porosity values are >10%, with MSs and WSs being the dominant sorting facies classes. In the North sector (Fig. 20), the Pss facies is dominant and porosity values are <17%; permeability values are <10 mD, and half of the values are <1 mD.

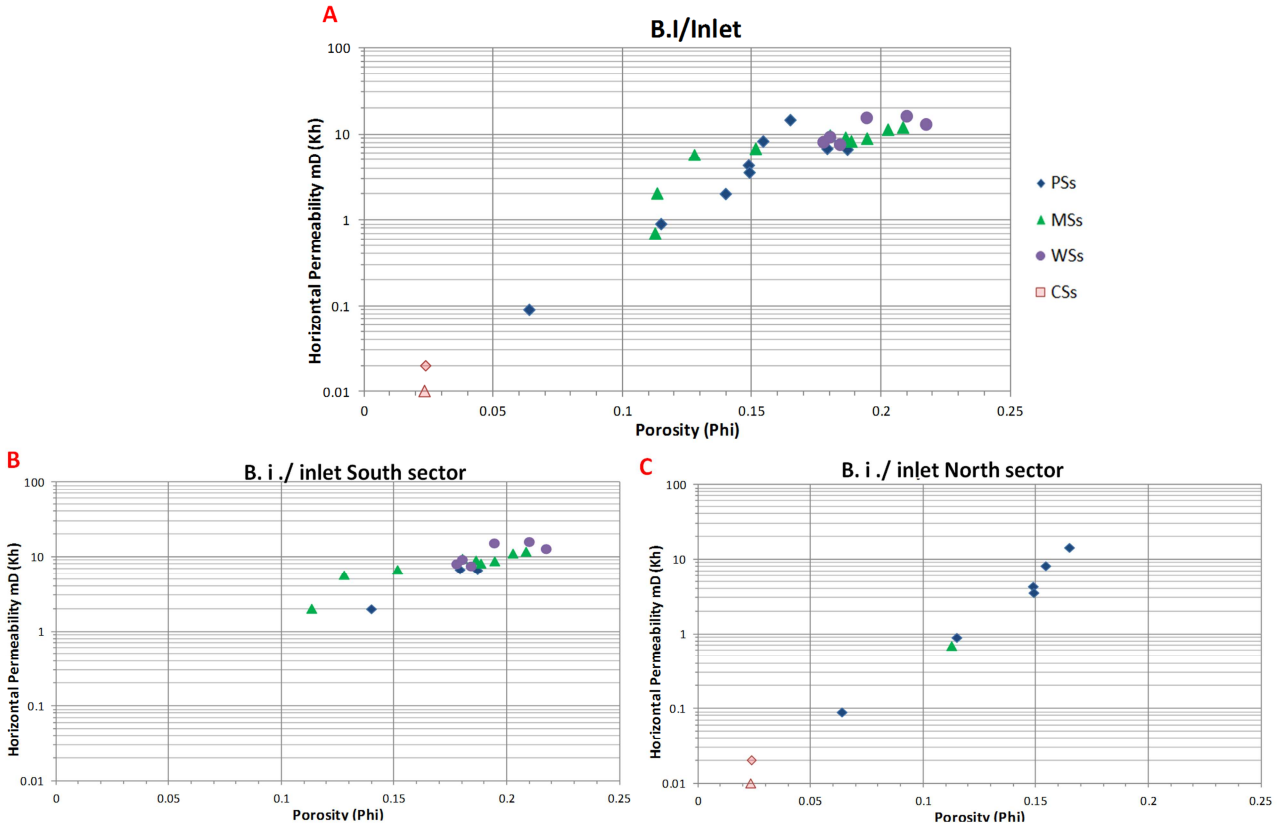

Fig. 20: Phi *versus* Kh plot for the b.i./inlet lithofacies, classified by sorting facies class. The cemented samples (CSs class) are shown by pale red symbols with the point shape representing the sub-classification of sample according to their sand sorting. (A) All samples. (B) Samples located at the South sector. (C) Samples located at the North sector.

Similarly, when samples are classified by grain-size facies class (Fig. 21), this plot shows two main grain-size facies classes, medium–coarse and fine–medium classes, representing samples with high Phi values (<17%). Plotting the samples for each sector profile, results show that in the South sector (Fig. 21A) Phi values are >10% and Kh values are >1 mD, and the dominant facies are fine–medium and medium–coarse grain-size classes. In the North sector (Fig. 21B), Phi is <17% and the dominant facies is the medium–coarse grain-size class.

A comparison of the Phi vs. Kh relationship for samples classified by sorting and cemented facies (Fig. 20) and those classified by grain size facies class (Fig. 21) shows that the correlation is stronger for the sorting and cemented facies, and that Phi values fall into at least three ranges that define the respective sorting and cemented facies: WSs, PSs and CSs. The porosity of the Wss facies is >17%; the porosity of the PSs facies, which is mainly located in the North sector (Fig. 20B), is <17%, while porosity values are lowest for the CSs facies (<5%). The porosity values for the MSs facies are 10%–22%.

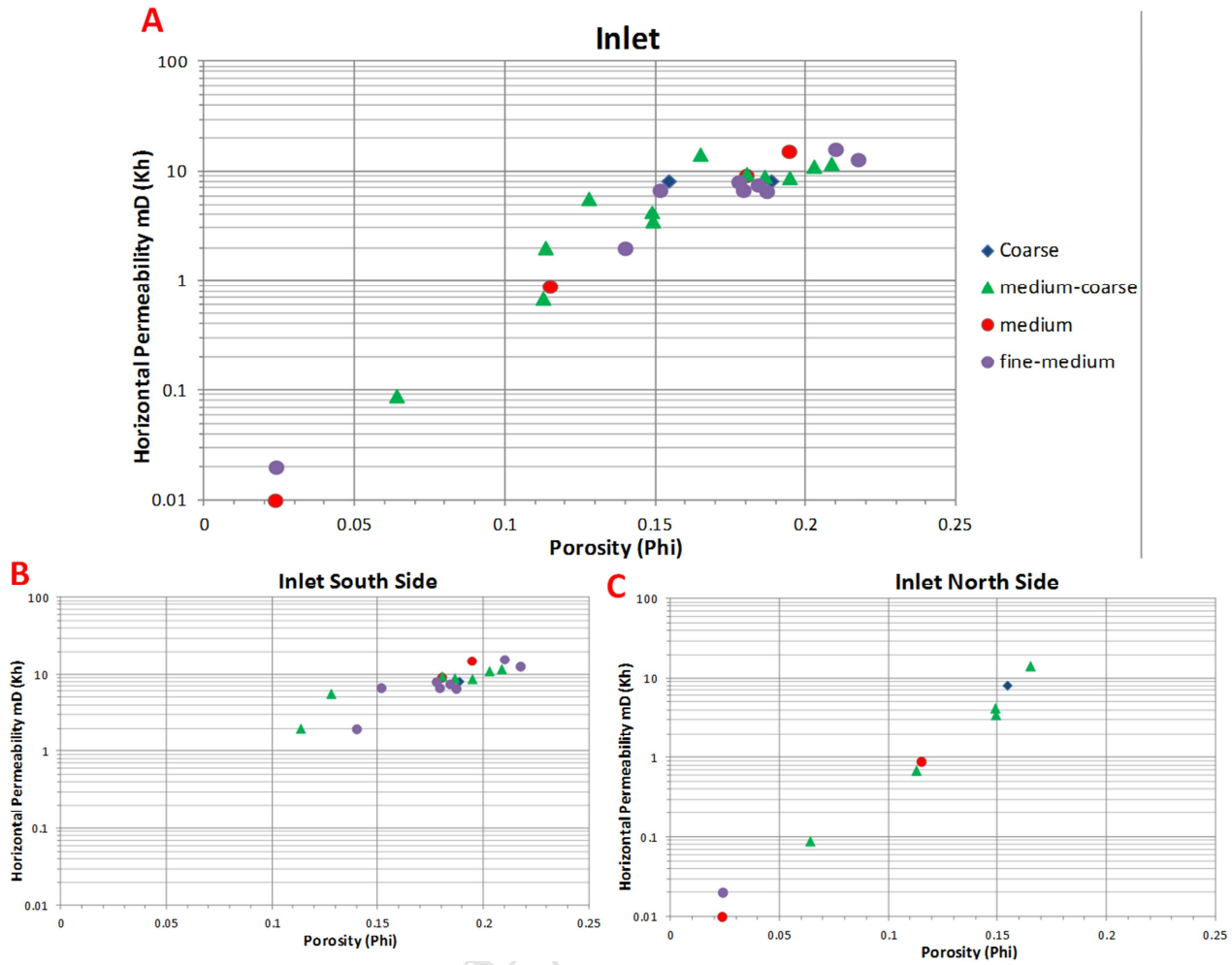

Fig. 21: Phi *versus* Kh plot for the b.i./inlet lithofacies, classified by grain-size facies class. (A) All samples. (B) Samples located at the South sector. (C) Samples located at the North sector.

6. Discussion

The study of the tsunami and b.i/inlet sandstone deposits at the mesoscopic (decimetre to tens of metres) and microscopic (millimetre to centimetre) scales in the Aliaga outcrop reservoir analogue has allowed us to identify and to distinguish different heterogeneities. A part of the mesoscopic scale heterogeneities, the main microscopic-scale heterogeneities of sandy facies were the variability in grain size, sorting of sand grains and cement content. From these diagnostic criteria, petrological analysis of samples in both deposits has allowed

their classification into different classes. Porosity and permeability measurements were obtained from samples previously classified according to sorting, grain-size and cement content criteria. Overall, the porosity and permeability results show a strong correlation in both deposits. In addition, the vertical permeability is strongly correlated with the horizontal one (Fig. 17). This correlation demonstrates the isotropic behaviour of permeability vectors. A low anisotropy of permeability in plug samples has also been noted by Meyer and Krause (2006) in samples without clay or carbonate laminae at millimetre scales; thus, the permeability anisotropy is likely to be dependent on the scale of the measurement. Our results also point to a stronger correlation of porosity and permeability with sorting facies than with grain-size facies, especially for the barrier island/inlet deposit (see Figs. 20 and 21). Porosity and permeability values obtained for two deposits are relatively low with respect to those normally involved in reservoirs; however, the two deposits behaved as a reservoir when CO_2 flow modelling was performed (Veloso, 2015). In the next sections, the results obtained for each deposit, the impact of cementation and the orders of heterogeneity, are discussed.

6.1. The tsunami reservoir

The tsunami deposit exhibits at the mesoscopic scale three main lithofacies that are homogeneously distributed within the sand geobody (Fig. 8). In drone photographs, two of them (LF2 and LF3) are indistinguishable from each other, and the third one (LF1) is recognized wherever its thickness exceeds 5 cm and its length is >1–2 m (Fig. 10). Lithofacies LF1 usually fills dinosaur tracks at the base of the North sector (Fig. 9B); this lithofacies is also preserved in an intermediate sedimentary succession at specific zones (Fig. 9B and D) without lateral continuity. Lithofacies LF2 is dominant in both sectors of the outcrop (Fig. 9B, D and E).

At the microscale, the tsunami deposit is composed of subarkosic–arkosic sandstones, with 70% of the samples belonging to the WSs and MSs sorting facies classes (Table 2); almost half the samples are classified in the fine–medium grain size class and the other half varies between medium, medium–coarse and coarse grain-size classes (Table 3). Generally, the lithofacies at mesoscopic scale are better correlated with grain size class than with sorting facies class. A comparison of facies in the North and South sectors shows that samples from the South sector are mainly represented by the WSs facies class whereas those of the North sector belong to the Wss and Mss facies classes, with some PSs facies samples. The porosity (Phi) and the horizontal permeability (Kh) of tsunami plugs vary within a range from 14% to 22% and 3 mD to 22 mD, respectively (Fig. 18), independently of sandy facies. Despite of the cementation in some samples, the Phi and Kh values lie within a narrow range.

The scarce variability of obtained results, and their relative no dependence of the sandy facies, can be probably link to the sedimentary processes involved during tsunami deposition. The distribution of sand in onshore tsunami deposits is usually complex, as tsunami run-up processes and the preservation of sediment depend on factors such as seabed and nearshore topography, and sediment source areas (Nanayama and Shigeno, 2006; Dawson and Stewart, 2007; Sugawara *et al.*, 2008; Martini *et al.*, 2010; Apotsos *et al.*, 2012; Phantuwongraj and Choowong, 2012; Sugawara *et al.*, 2014). At geological time scales, tsunami deposits occur instantaneously, as single sedimentary events (Fujiwara and Kamataki, 2007). According to the sedimentological and architectural features described by Navarrete *et al.* (2014), the studied deposit is an onshore multiple-bed tsunami sandstone (Fujiwara, 2008), in which the five fining-upwards facies-sequences correspond to successive incursions and outflows of the tsunami wave train. The scarce variability in the petrophysical behaviour of the tsunami sandstones must be related to those factors responsible for its

lateral and vertical facies homogeneity. Among these, the sand source, the dynamics of the deposition process and the antecedent topography probably were the most important controlling factors. The source for sand was mainly the erosion and reworking of barrier island sand (Navarrete *et al.* 2014), which probably had a certain grade of sandy facies homogeneity, as it has been shown for the studied barrier island/inlet deposit. In addition, the main process during deposition was particle settling from the tsunami hyperconcentrated flow. Particle settling was driven by grain density; so, due to sand compositional homogeneity, it was mainly controlled by particle grain-size. Thus, this deposition process determined a further homogeneous sand facies distribution. The flat-lying antecedent topography interpreted by Navarrete *et al*. (2014) also could contribute to a low diversity in sand facies. It probably determined a laminar flow, more than a turbulent flow, in the lagoon depositional area, contributing then to a more homogeneous particle settling process.

A comparison of the Aliaga tsunami deposit and two Holocene deposits from recent tsunami waves outlines some differences and similarities of their sand facies at three scale of observation (Table 7). One of the Holocene deposits was described by Nanayama and Shigeno (2006) in southwestern Hokkaido, northern Japan, at the Taisei coast. It is an onshore deposit caused by a magnitude 7.8 earthquake along the Japan coast in 1993. The deposit is composed of two lithofacies, a gravel lobe facies (GLF) and a sand-sheet facies (SSF), organized into two fining-upwards sequences, and whose upper sequence is more widely distributed and thicker than the lower sequence The upper sequence is coarser grained than the lower sequence, as the second run-up was larger than the first. Other Holocene deposit was described by Matsumoto *et al.* (2010) in and around Periya Kalapuwa Lagoon, Sri Lanka. The tsunami wave was caused by Indian Ocean tsunami in 2004. The Kalapuwa tsunami deposits consist of well-sorted fine–coarse sand. The landward extent of the Kalapuwa deposits is greater along two

transects near two inlets (~1000 m long in each case), suggesting that tsunami deposition was controlled by run-up flow through the inlets.

Table 7: Comparison of the tsunami deposits of Aliaga and Taisei (Nanayama and Shigeno, 2006) and Kalapuwa (Matsumoto *et al.,* 2010) locations. Table headings: 'Differences and Similarities' are the main differences and similarities between Aliaga and other deposits; 'Tsunami deposit' is the location of the deposit; 'Series' is the Geological Period of the deposit sedimentation; 'Regional, Mesoscopic and Microscopic' are the scale of observation of the main differences and similarities between the deposits.

	Differences			
Tsunami deposit	**Series**	**Regional (hundred of meters to kilometres)**	**Mesoscopic (decimetre to tens of metres)**	**Microscopic (millimetre to centimetre)**
Taisei (Nanayama and Shigeno, 2006)	Holocene	- 0-460 m from coast line - Deposited in the river	2 lithofacies	- Dominant fine-grained - Upper layers coarse-grained - No mention about cementation
Aliaga	Lower Cretaceous	- 5-8 km from coast line - Deposited in the mud flats and carbonate lagoon	3 lithofacies	-20% of cemented facies - Fine-to coarse grained facies - Upper layers fine-grained
Kalapuwa (Matsumoto *et al.*, 2010)	Holocene	- 0-1000 m from coast line - Deposited in the lagoon and inlet		No mention about cementation
	Similarities			
Tsunami deposits	**Series**	**Regional (hundred of meters to kms)**	**Mesoscopic (decimetre to metre)**	**Microscopic (millimetre to centimetre)**
Aliaga – Taisei		Onshore	- Outflow event - Upper facies-sequence widely distributed and thicker	- Wss and MSs is dominant facies - Fining-upwards facies-sequences
Aliaga - Kalapuwa		Sediment source from sand dunes	Graded bedding structures	- WSs facies is dominant - Fine-to coarse grained

The main difference between the Aliaga deposit and the Taisei and Kalapuwa deposits at the regional scale is the distance of deposition from the coastline (Table 7). At the mesoscopic and microscopic scales, the facies are also different between deposits in terms of numbers of

facies-sequences, grain size distribution and cement content. Despite of the differences in sand facies between the deposits, the sand grains are well- to moderately-sorted in the three deposits. The homogeneous texture of well-sorted sand grains is independent of the grain-size distribution (Matsumoto *et al.*, 2010; Sun *et al.*, 2007). Moreover the distribution of porosity and permeability values of the Aliaga tsunami is relatively homogenous, with a range of porosity from 14% to 22% and permeability from 3 mD to 22 mD (Fig.). Porosity and permeability data in other tsunami deposits around the world were not found.

Finally, the Aliaga tsunami deposit is a single and instantaneous event considering the geological time scale. The dominant sedimentary process was a turbidity flow, which deposited sand sediments from the sand barrier principally through backflow currents of the tsunami wave train. The homogeneity of sedimentary process controlled the homogenous sorting of sand and hence the porosity distribution, despite of the variability in sand grain size.

6.2. The b.i./inlet deposit reservoir

At the mesoscopic scale, two main lithofacies are recognized in the b.i./inlet sand geobody with a marked inhomogeneous spatial distribution. In the South sector (Fig. 12A) a thick LF4 lithofacies (ochre-coloured medium- to fine-grained sandstone) is dominant. In the North sector (Fig. 12B), lithofacies LF5 (a grey cemented sandstone with local drapes) also appear. At the microscale, the b.i./inlet deposit is composed of subarkosic–arkosic sandstones, and differences between the North and South sectors are found in the distribution of sorting and cemented facies (Fig. 12, Table 5); the WSs and MSs facies are abundant in the South sector (Fig. 12A) whereas the PSs and CSs facies are abundant in the North sector (Fig. 12B). The porosity (ranging from 0 to 22%) and permeability (ranging from 0 to 22 mD) are better correlated with sorting facies than with grain-size facies (Fig. 20). In any case, the porosity

and permeability values are higher in the South sector than in the North sector (Fig. 20, Table 8).

Table 8: Measured porosity intervals in the b.i./inlet deposit in both outcrop sectors and grouped by sorting and cemented facies. The facies fraction is the percentage of samples for a given facies in each sector.

Sorting Facies class	CSs	PSs	MSs	WSs
Porosity interval (%)	0-6	6-17	11-21	17-22
Facies Fraction in North sector	100%	66%	10%	0%
Facies Fraction in South sector	0%	33%	90%	100%

The studied b.i./inlet deposit was deposited in a back barrier system composed of a barrier island and tidal inlet (Navarrete *et al.*, 2013a). Inlet deposits associated with barrier-island systems are typically represented by complex fill patterns marked by multiple episodes of erosion, lateral filling and migration of the system (Mallinson *et al.*, 2010, Nishikawa and Ito, 2000). Heterogeneity in distribution of sand facies is determined first by the processes dominant in the barrier systems, and secondarily by the architectural elements of such systems (Davis and Barnard, 2003; Simms *et al.*, 2006; Hodgkinson *et al.*, 2008; Mallinson *et al.*, 2010). The inlet deposits change dynamically and complexly through time, and their evolution depends on the dominant process (wave-dominant or tidal-dominant) and the interactions between processes (Davis and Gibeaut, 1990; Davis and Barnard, 2000; Nishikawa and Ito, 2000; Simms *et al.*, 2006; Navarrete *et al.*, 2013a). In the South sector of the Aliaga outcrop, lithofacies LF4 (Fig. 11A and B) was generated by migration of minor megaripples moved by flood and ebb water fluxes (Navarrete *et al.*, 2013) that promoted the development of straight sinuous crest ripples from the sandy bedload (Collison, 1996; Miall, 1996; Ghazi and Mountney, 2009) under a low-energy flow regime in the shoreface zone of

the tidal inlet/barrier spit (Navarrete *et al.*, 2013a). These low-energy processes deposited and preserved homogeneous and usually well or moderately sorted sand (Table 5). Whereas in the North sector, the existence of drapes formed by carbonaceous plant fragments and asymmetric wave and interference ripple structures (Fig. 10C and D) indicates variations in the flow regime, probably associated with tidal flows from brackish to marine conditions (Navarrete *et al.*, 2013a). The variations in flow regime, the mixing conditions and properties of water in the system, resulted generally in a poorly-sorted sand, with locally important cementation (Table 5).

A comparison of the characteristics of the studied b.i./inlet deposit with the Upper Cretaceous outcrop of inlet deposits associated to barrier-island described by Jackson and Rawn-Schatzinger (1993) shows similarities in the distribution and lithology of facies (Table 9) over a similar distance of 165 meters. The distribution and lithology of facies is related to lateral migration of the tidal inlets and their tidal energy flux, sand sources and channel configuration (Jackson and Rawn-Schatzinger, 1993). In the North sector of Aliaga outcrop, the studied deposit is composed of sand facies, which are similar to the inlet-infill facies characterized by Jackson and Rawn-Schatzinger (1993). The inlet-infill facies consisted of coarser-grained sandstone and more poorly-sorted sandstone than the facies of tidal channel. The facies of tidal-channel are composed of finer-grained and moderately to well-sorted sandstone, such as the facies in the South sector of studied b.i./inlet deposit. The difference of facies distribution between sectors of outcrop is mainly related to the sedimentary nature of the deposit. Conditions and changes of inlet flow in the dominant process drive facies heterogeneity into the deposit, and consequently the spatial distribution of sorting facies and porosity.

Table 9: Comparison of the studied b.i./inlet deposit and the inlet deposit described by Jackson and Rawn-Schatzinger (1993). Table headings: 'Similarities' are the main differences and similarities between deposits and other deposit; 'Series' is the Geological period of the sediment deposition; 'Regional, Mesoscopic and Microscopic' is the scale of observation of the main similarities between deposits.

	Similarities			
	Series	**Regional (hundred of meters to km)**	**Mesoscopic (decimetre to metre)**	**Microscopic (millimetre to centimetre)**
Aliaga - Almond Fm. (Jackson and Rawn-Schatzinger, 1993)	Cretaceous	Barrier island and associated inlet deposits	2 lithofacies	- A coarser-grained and poorly sorted facies (Inlet-infill facies or LF5) - A finer-grained and moderately to well-sorted facies (tidal-channel facies or LF4) - presence of the dolomite cement

The distribution of porosity and permeability values of the b.i./inlet deposit has a strong relationship with distribution of sorting and cemented facies (see below). The porosity varies according to facies, where the higher porosity values correspond to the well-sorted facies and the lower porosity values correspond to the poorly-sorted and cemented facies. The porosity and permeability distributions reflect the sedimentary heterogeneity observed in each sector of the profile. The permeability variation of studied deposit is consistent with the permeability heterogeneity observed by Ambrose *et al.* (2008) for reservoirs in beach and barrier-island systems in the West Ranch field (Gulf Coast, USA). Over an area of 165 m^2 and thickness of 3.3 m, these authors described permeability variations in the inlet infill facies of up to three orders of magnitude (<500 to 1000 mD), whereas permeability values in the barrier-core facies display less variability, with the highest permeability occurring at the top of the succession (>2000 mD).

6.3. Impact of cementation

Some zones in the tsunami and b.i./inlet deposits are cemented. The cement is principally kaolin and calcite and locally dolomite; which are filling the pore space, as observed by Caja (2004) and Bauluz *et al.* (2014). Cementation could be responsible of the low permeability magnitude of samples (up to 20 mD).

Both deposits are arkose to sub-arkose sandstones, and the kaolin cement could crystallize from a fluid rich in Si and Al cations, which is a result of silicate alterations, such as feldspars. The process to crystallize kaolinite might have started prior to the diagenesis but it continued and reached a maximum of crystallization during diagenesis (Bauluz *et al.*, 2014). Hammer *et al.* (2010), who described cementation in the Upper Triassic–Lower Jurassic Åre Fm., also demonstrated a link between compaction, diagenesis and kaolin cementation. The authigenic kaolinite observed by Hammer *et al.* (2010) is the only pore-filling clay mineral, and in some places its volume exceeds 10% of the total rock volume. The kaolinite is interpreted to have formed both by replacement through leaching of feldspar and mica, and by eogenetic precipitation from pore fluids. The effect of cementation on reservoir quality is relatively limited, as cementation is restricted to millimetre-scale laminae of mica and organic debris (Hammer *et al.,* 2010).

The carbonate cementation in both deposits can be related to burial processes (Curtis, 1978) and/or early diagenesis (Machent *et al.*, 2007; Henares *et al*., 2014). There, early non-ferroan calcite precipitates first with solutes derived from marine water and sulphate reduction, which is very common in transgressive shallow marine–coastal plain deposits during relative sea-level rise and flooding (Machent *et al.*, 2007). Early diagenesis also probably induced early compaction and consolidation of barrier sequences (deVries Klein, 1974). The cemented facies (CSs) in the tsunami deposit of the present study is sparsely distributed. The cementation may exhibit reduced porosity and permeability to levels that are within the

tsunami porosity range (14%–22%) but which would be higher in the absence of cementation (Henares *et al.* 2014). In inlet deposits associated with barrier islands, Jackson and Rawn-Schatzinger (1993) observed large amounts of calcite cement in oyster-rich beds.

The cement of the studied b.i./inlet deposit is principally dolomite, particularly affecting the lithofacies LF5, and strongly reduces porosity and permeability (Fig. 20). The lithofacies LF5 contains scattered oysters, fish teeth and centimetre-thick accumulations of bioclasts or carbonaceous plant fragments. The dolomite cementation may also be related to fluid migration through fractures and faults. Syn-sedimentary activity related to extensional structures in the Cretaceous Galve sub-basin has been highlighted in previous studies (Soria, 1997; Liesa *et al.*, 2004, 2006; Navarrete *et al.*, 2013a, 2013b), and such structures could have acted as preferred pathways for fluid remobilization during and after compaction. Martín-Martín *et al.* (2012) examined dolomite bodies occurring in association with basement faults in the southeast Maestrazgo Basin. The dolomites appear to be intercalated with very low-porosity mud-dominated facies and/or early cemented grain-dominated facies. Most of the dolostone volume (60%–70%) consists of replaced dolomite showing characteristic fabric-retentive textures and low porosities. The dolomitization was controlled primarily by tectonic structures in the area, and secondarily by depositional fabrics and early diagenetic processes. The fluid flow pattern through strata and along faults could be part of a larger scale convective system that may have been active in the Maestrazgo basin during the Late Cretaceous post-rift episode (Martín-Martín *et al.*, 2015).

6.4. Orders of sedimentary heterogeneity

The heterogeneity of facies in the tsunami deposit and b.i./inlet deposit is primarily a function of the observation scale and secondarily of the sedimentary processes. Both sand deposits are continuous over a vast extent and are composed of fine to coarse sandstones deposited in a

sedimentary system of back barrier-island. However, each deposit has a particularly distribution of facies and petrophysic properties. The sand and petrophysics heterogeneities between deposits are important at the metre scale and are very important at the centimetre scale. The genesis and conditions of sandstone deposition generated the distribution of sand heterogeneity, at both the mesoscopic and the microscopic scale. The tsunami deposit is a single sedimentary event deposited principally by backflow currents under good sedimentary conditions for its preservation. The b.i./inlet deposit is a complex combination of sediment erosion, reworking and preservation under distinct and dynamic flow conditions. Samples from the tsunami deposit are relatively homogeneous in terms of the sorting facies (70% composed of WSs and MSs facies) and porosity distribution (14-22%) whereas the b.i./inlet samples have heterogeneous distribution of sorting facies into the deposit. In the b.i./inlet deposit, the distribution of sorting and cemented facies is strong correlate to the distribution of the porosity values.

The sand heterogeneity correlated to the petrophysic properties of both deposits can be hierarchically ordered as a function of the scale of observation (Fig. 22). First-order heterogeneity is related to observation at the basin scale; the sand heterogeneity between deposits is undistinguished at this scale, as both sand geobobys appear as hogeneous sand beds laterally continuous. Second-order heterogeneity is related to genesis and the conditions of sediment deposition and preservation; these heterogeneities can be recognized at the meter scale, and can be important at the millimetre scale. The facies and petrophysic properties distribution is mainly controlled by the genesis of sandstone deposit, thus the heterogeneity of second-order describes the petrophysic variability of sand facies. Third-order heterogeneity is related to post-sedimentation events, such as cementation from compaction and diagenesis, which can locally or globally change the petrophysic properties of

sand facies in the deposit. Heterogeneity of third order are also related to the presence of syn-sedimentary faults and/or palaeo-relief which can locally change the flow conditions (Pochat and Van Den Driessche, 2007) and/or the accommodation space (García-García *et al.*, 2006; Foix *et al.*, 2013; Navarrete *et al.*, 2013a), and therefore can affect the distribution of sand facies in the deposit. Moreover syn-sedimentary faults may play an important role in fluid remobilization during compaction and diagenesis, as well as in deeper conditions as conduct or barrier to fluid flow. The intense cementation in the North sector of b.i./inlet deposit seems to be related to the proximity with the Remenderuelas and other minor associated syn-sedimentary normal faults, and to the inlet infill nature of facies in this sector.

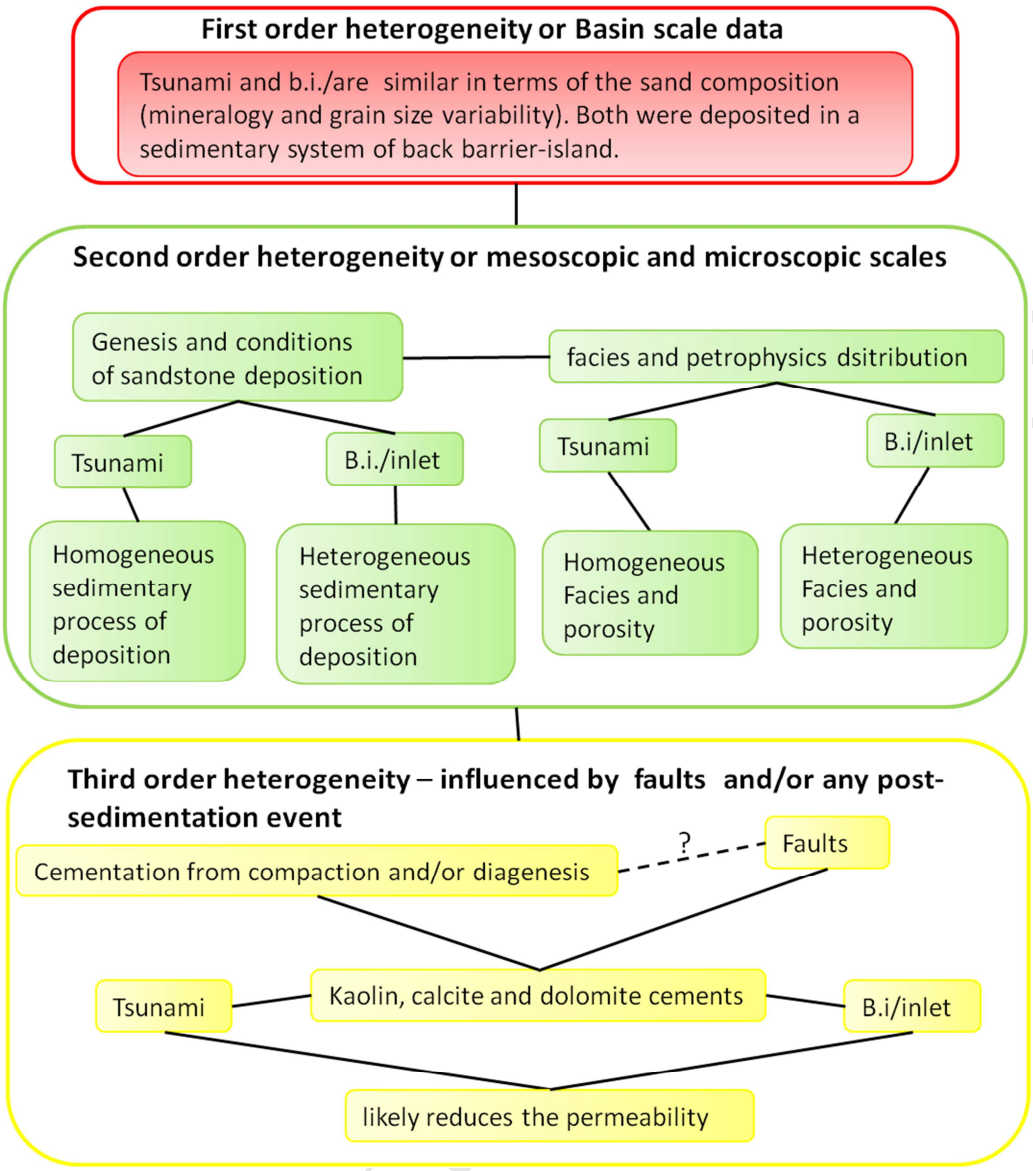

Fig. 22: The hierarchy of sand heterogeneity correlated to the petrophysics of both deposits as a function of the scale of observation.

7. Conclusions

The depositional processes of the studied tsunami and barrier island/inlet sandstone deposits control the grain-size and sorting of sandy facies, as well as their lateral variability. These factors, together with the early or late cementation of facies, control the distribution of petrophysical characteristics. Despite the small size of the outcrop, the two studied deposits

show distinct sedimentary processes under the same palaeogeographical context, as well as distinct petrophysical properties. The sorting facies classification seems to be more appropriate for describing sand heterogeneity related with petrophysics, although cementation must be also take into account.

Despite of the important variation in sand grain-size (coarse to fine) of the tsunami deposit, the sand sorting is moderated to well, and the porosity variation is low (14-22%). The sedimentary processes that took place during tsunami deposition, mainly the original characteristics of source sand, the sedimentation from settling, and a laminar flow, controlled the homogenous sorting of sand and hence the porosity distribution, despite of the variability in sand grain size.

The barrier island-tidal inlet deposit is composed of inlet-infill facies in the North sector and tidal-channel facies in the South sector. In the North sector, the sand is poor-sorted and the cementation is important, whereas in the South sector, the sand is moderate-sorted and the cementation is low. In an extension of 200m in length, the deposit showed significant variation in facies and petrophysics. Inlet deposits are characterized by multiple episodes of erosion, migration and lateral filling of inlets within the barrier island system, therefore, the heterogeneous distribution of porosity reflects the heterogeneous nature of the deposition process.

Porosity and permeability are strongly correlated in both sandstone deposits.

The sand heterogeneity related to the petrophysics in both deposits can be hierarchically ordered as a function of the scale of observation. The heterogeneity of sand facies in the tsunami deposit and the b.i./inlet deposit is primarily a function of the observation scale and secondarily of the sedimentary processes

The hierarchy of sand heterogeneity can be applied in reservoir studies of clastic back barrier sedimentary systems, especially in tsunami and barrier- island and associated inlet deposits.

In reservoir studies, the second-order heterogeneity is assessed through sedimentological studies of seismic, core and well logs data. The sedimentary model can be improved through the study of analogous outcrop and the up-scaling of outcrop characteristics into reservoir model. The use of analogous outcrops bridges the inter-well-scale gap that is generally used to define the spatial variability of reservoir properties (White *et al.*, 2004), such as facies and petrophysics. A most likely and realist reservoir model depends on the knowledge of sedimentary model and on the correlation between the sedimentology and petrophysics. The good correlation between facies and petrophysic properties allowed to performer the petrophyscical modelling as a function of facies model, and to produce geologically realist spatial distributions of porosity and permeability in the reservoir. The third-order heterogeneity in reservoir studies is assessed through studies of tectonic and its relationship with cementation. Faults could serve as conduct to fluid remobilization during and after compaction and/or diagenesis. The remobilized fluid could precipitate or dissolve cements in the sandstone deposits and change initial porosity and/or permeability linked to the genesis of sand facies.

8. Acknowledgements

The authors gratefully acknowledge Carlos Luis Liesa Carrera for the useful comments to the previous manuscript. The reviewers Sudipta Dasgupta and César Viseras, and the associate editor Luis Buatois are thanked for critically reviewing, and greatly improving this manuscript. This research is a contribution to the project: Análisis de Cuencas Sedimentarias Continentales, of the Gobierno de Aragón, the Análisis de Cuencas Sedimentarias Group of the

UCM-CAM, and the projects CGL2011-23717 (Ministerio de Ciencia e Innovación of the Spanish Government and FEDER) and UZ2015-CIE-10 (University of Zaragoza). Additional financial support was provided by a Cnpq (Conselho Nacional de Pesquisa e Desenvolvimento Tecnologico, Brasil) Research Grant and an IAS 2014 Postgraduate Grant to F. Veloso.

9. References

AAPG (American Association of Petroleum Geologist), 2015. AAPG Wiki accessed in July, 2015. website: ttp://wiki.aapg.org/Main_Page.

Alvaro, M., Capote, R., Vegas. R., 1979. Un modelo de evolución geotectónica para la Cadena Celtibérica. *Acta Geológica Hispanica* 14, 172–177.

Ambrose, W.A., Lakshminarasimhan, S., Holtz, M.H., Núñez-López, V., Hovorka, S.D., Duncan, I., 2008. Geologic factors controlling CO2 storage capacity and permanence: case studies based on experience with heterogeneity in oil and gas reservoirs applied to CO2 storage. *Environmental Geology* 54, 1619–1633.

Apotsos, A., Gelfenbaum, G., Jaffe, B., 2012. Time-dependent onshore tsunami response. *Coastal Engineering* 64, 73–86.

Antolín-Tomás, B., Liesa, C.L., Casas, A.M., Gil-Peña, I., 2007. Geometry of fracturing linked to extension and basin formation in the Maestrazgo basin (Eastern Iberian Chain, Spain). *Revista de la Sociedad Geológica de España* 20, 3-4, 351-365.

Asharf, M., 2014. Geological storage of CO2: Heterogeneity impact on the behaviorof pressure. *International Journal of Greenhouse Gas Control* 28, 356–368.

Bachu, S., Bonijoly, D., Bradshaw, J., Burruss, R., Holloway, S., Christensen, N.P., Mathiassen, O.M., 2007. CO2 storage capacity estimation: Methodology and gaps. *International journal of greenhouse gas control* 1, 430–443.

Bauluz, B., Yuste, A., Mayayo, M. J., Canudo, J. I., 2014. Early kaolinization of detrital Weald facies in the Galve Sub-basin (Central Iberian Chain, north-east Spain) and its relationship to palaeoclimate. *Cretaceous Research* 50, 214-227.

Bondevik, S., Svendsen, J.I., Mangerud, J., 1997. Tsunami sedimentary facies deposited by the Storegga tsunami in shallow marine basins and coastal lakes, western Norway. Sedimentology 44, 1115–1131.

Caja, M.A., 2004. *Procedencia y diagénesis de los sedimentos del Jurásico superior-Cretácico inferior (facies Weald) en las subcuencas occidentales de la Cuenca del Maestrazgo, Cordillera Ibérica Oriental*. Tesis Doctoral, Univ. Complutense de Madrid, 293 p.

Capote, R., Muñoz, J.A., Simón, J.L., Liesa, C.L., Arlegui, L.E., 2002. Alpine tectonics I: the Alpine system north of the Betic Cordillera. In: Gibbons, W., Moreno, T. (eds), *Geology of Spain*. The Geological Society, London, 367–400.

Collison, J.D., 1996. Alluvial sediments. In: Reading, H.G. (ed), *Sedimentary Environments and Facies*. Blackwell Publishing, Oxford, 37–82.

Corbett, P.W.M., Potter, D.K., 2004. Petrotyping: a basemap and atlas for navigating through permeability and porosity data for reservoir comparison and permeability prediction. International Symposium of the Society of Core Analysts, Abu Dhabi, UAE, 5-9 October.

Curtis, C.D., 1978. Possible links between sandstone diagenesis and depth-related geochemical reactions occurring in enclosing mudstones. *Journal of the Geological Society* 135(1), 107-117.

Cushman, J.H., 1997. *The Physics of Fluids in Hierarchical Porous Media: Angstroms to Miles*. Springer, Heidelberg. 484 p.

Dalrymple, M., 2001. Fluvial reservoir architecture in the Statfjord Formation (northern North Sea) augmented by outcrop analogue statistics. *Petroleum Geoscience* 7, 115-122.

Davis, R.A., Gibeaut, J.C., 1990. Historical Morphodynamics of Inlets in Florida: *Models for Coastal Zone Planning*. Tech Paper 55. Florida Sea Grant College, Gainesville, FL, 81 p.

Davis, R.A., Barnard, P.L., 2000. How anthropogenic factors in the back-barrier area influence tidal inlet stability: examples from the Gulf Coast of Florida, U.S.A. In: Pye, K., Allen, J.R.L. (eds), *Coastal and Estuarine Environments: Sedimentology, Geomorphology and Geoarchaeology*. Geol. Soc. London Spec. Publ. 175, 293-303.

Davis, R.A., Barnard, P.L., 2003. Morphodynamics of the barrier-inlet system, west-central Florida. *Marine Geology* 200, 77-101.

Dawson, A. G., Stewart, I., 2007. Tsunami deposits in the geological record. *Sedimentary Geology* 200, 3, 166-183.

DeVries Klein, G., 1974. Estimating water depths from analysis of barrier island and deltaic sedimentary sequences. *Geology* 2, 8, 409-412.

Donselaar, M.E., 1996. Barrier island coasts and relative sea level rise: preservation potential, facies architecture and sequence analysis. PhD. Thesis. Utrecht University. 223 pp.

Eaton, T.T., 2006. On the importance of geological heterogeneity for flow simulation. *Sedimentary Geology* 184, 187–201.

Ekeland, A., Pedersen, N., Howell, J., Nemec, W., Keogh, K., Viste, I., 2008. Modeling of Intra-Channel Belt Depositional Architecture in Fluvial Reservoir Analogs from the Lourinha Formation, Portugal. *Search and Discovery Article* number: 50146.

Folk, R.L., 1980. *Petrology of Sedimentary Rocks*. Hemphill Publish Company. Austin, USA. 184 p.

Foix, N., Paredes, J.M., Giacosa, R.E., 2013. Fluvial architecture variations linked to changes in accommodation space: Río Chico Formation (Late Paleocene), Golfo San Jorge basin, Argentina. *Sedimentary Geology* 294, 342–355.

Frykman, P., 2009. The importance of geological heterogeneities. CO2GeoNet Open Forum March 18-20, Venice, San Servolo Island, Italy.

Frykman, F., Nielsen, C.M., Bech, N., 2013. Trapping effects of small scale sedimentary heterogeneities. *Energy Procedia* 37, 5352 – 5359.

Fujiwara, O., 2008. Bedforms and sedimentary structures characterizing tsunami deposits. In: Shiki, T., Tsuji, Y., Yamazaki, T., Minoura, K. (eds), *Tsunamiites — Features and Implications*. Elsevier, Amsterdam, Oxford, 51–62.

Fujiwara, O., Kamataki, T., 2007. Identification of tsunami deposits considering the tsunami waveform: an example of subaqueous tsunami deposits in Holocene shallow bay on southern Boso Peninsula, Central Japan. *Sedimentary Geology* 200, 3, 295-313.

García-García, F., Ferñandez, J., Viseras, C., Soria, J.M., 2006. Architecture and sedimentary facies evolution in a delta stack controlled by fault growth (Betic Cordillera, southern Spain, late Tortonian). *Sedimentary Geology* 185, 79 – 92.

Ghazi, S., Mountney, N.P., 2009. Facies and architectural element analysis of a meandering fluvial succession: the Permian Warchha Sandstone, Salt Range, Pakistan. *Sedimentary Geology* 221, 99–126.

Guimerà, J., Salas, R., Vergés, J., Casas, A., 1996. Extensión mesozoica e inversión compresiva terciaria en la Cadena Ibérica: aportaciones a partir del análisis de un perfil gravimétrico. *Geogaceta* 20 , 7, 7697-7694.

Hammer, E., Mørk, M.B.E., Næss, A., 2010. Facies controls on the distribution of diagenesis and compaction in fluvial-deltaic deposits. *Marine and Petroleum Geology*, 27, 8, 1737-1751.

Heinz, J., Kleineidam, S., Teutsch, G., Aigner, T., 2003. Heterogeneity patterns of Quaternary glaciofluvial gravel bodies (SWGermany): application to hydrogeology. *Sedimentary Geology* 158, 1–23.

Henares, S., Caracciolo, L., Cultrone, G., Fernández, J., Viseras, C., 2014. The role of diagenesis and depositional facies on pore system evolution in a Triassic outcrop analogue (SE Spain). *Marine and Petroleum Geology* 51, 136-151.

Hodgkinson, J., Cox, M.E, McLoughlin, S., Huftile, G.J., 2008. Lithological heterogeneity in a back-barrier sand island: Implications for modelling hydrogeological frameworks. *Sedimentary Geology* 203, 64–86.

Hornung, J., Aigner, T., 1999. Reservoir and aquifer characterization of fluvial architectural elements: Stubensandstein, Upper Triassic, southwest Germany. *Sedimentary Geology* 129, 215–280.

Huysmans, M., Peeters, L., Moermans, G., Dassargues, A., 2008. Relating small-scale sedimentary structures and permeability in a cross-bedded aquifer. *Journal of Hydrology* 361, 41– 51.

IFP (Instituto Petrofísico de Madrid), 2012. Helium Porosity and Permeability measurements. Technical Report.

Issautier, B., Viseur, S., Audigane, P., le Nindre, Y.M., 2014. Impacts of fluvial reservoir heterogeneity on connectivity: Implications in estimating geological storage capacity for CO2. *International Journal of Greenhouse Gas Control* 20, 333–349.

Jackson, S.R., Rawn-Schatzinger, V., 1993. Data from selected Almond Formation outcrops--Sweetwater County, Wyoming (No. NIPER--724). National Inst. for Petroleum and Energy Research, Bartlesville, OK (United States).

Klingbeil, R., Kleineidam, S., Asprion, U., Aigner, T., Teutsch, G., 1999. Relating lithofacies to hydrofacies: outcrop-based hydrogeological characterisation of quaternary gravel deposits. *Sedimentary Geology* 129, 3-4, 299–310.

Kumar, N., Sanders, J.E., 1974. Inlet sequence: a vertical succession of sedimentary structures and textures created by the lateral migration of tidal inlets. Sedimentology 21, 491–532.

Lantuéjoul, C., Beucher, H., Chilès, J.P., Lajaunie, C., Wackernagel, H., Elion, P., 2005. Estimating the trace length distribution of fractures from line sampling data. In Leuangthong, O., Deutsch, C. V. (eds), *Geostatistics Banff 2004*. Quantitative Geology and Geostatistics 14, 165–174. Springer Netherlands, Dordrecht.

Liesa, C., Soria, A.R., Meléndez, A., 2000. Lacustrine evolution in a basin controlled by extensional faults: the Galve subbasin, Teruel, Spain. In: Gierlowski-Kordesch, E.H., Kelts, K.R. (eds), *Lake Basins through Space and Time*. American Association of Petroleum Geologists, Studies in Geology, 46, 295–302.

Liesa, C.L., Casas, A.M., Soria, A.R., Simón, J.L., Meléndez, A., 2004. Estructura extensional cretácica e inversión terciaria en la región Aliaga-Montalbán. In: Colombo, F., Liesa,C.L., Meléndez, G., Pocoví, A., Sancho, C., Soria, A.R. (eds), *Itinerarios Geológicos por Aragón*. Sociedad Geológica de España, Geo-Guías 1, 151–180.

Liesa, C.L., Soria, A.R., Meléndez, N., Meléndez, A., 2006. Extensional fault control on the sedimentation patterns in a continental rift basin: El Castellar Formation, Galve sub-basin, Spain. *Geological Society of London* 163, 487–498.

Lowe, D.R., 1982. Sediment gravity flows: II. Depositional model with special reference to the deposits of high-density turbidity currents. Journal of Sedimentary Petrology 52, 279–297.

Machent, P.G., Taylor, K.G., Macquaker, J.H.,Marshall, J.D., 2007. Patterns of early post-depositional and burial cementation in distal shallow-marine sandstones: Upper Cretaceous Kenilworth Member, Book Cliffs, Utah, USA. *Sedimentary Geology* 198, 1, 125-145.

Mallinson, D.J., Smith, C.W., Culver, S.J., Riggs, S.R., Ames, D., 2010. Geological characteristics and spatial distribution of paleo-inlet channels beneath the outer banks barrier islands, North Carolina, USA. Estuarine, *Coastal and Shelf Science* 88, 175-189.

Martín-Martín, J.D., Gómez Rivas, E., Travé i Herrero, A., Salas, R., Vergés, J., 2012. Dolomías controladas por fracturas en carbonatos aptienses de la zona de Benicàssim (SE Cuenca del Maestrat): distribución y características petrográficas. *Geogaceta* 51, 19-22.

Martín-Martín, J. D., Travé, A., Gomez-Rivas, E., Salas, R., Sizun, J. P., Vergés, J., Alfonso, P., 2015. Fault-controlled and stratabound dolostones in the Late Aptian–earliest Albian Benassal Formation (Maestrat Basin, E Spain): Petrology and geochemistry constrains. *Marine and Petroleum Geology* 65, 83-102.

Martini, P.M., Barbano, M.S., Smedile, A., Gerardi, F., Pantosti, D., Del Carlo, P. , Pirrotta, C., 2010. A unique 4000 year long geological record of multiple tsunami inundations in the Augusta Bay (eastern Sicily, Italy). *Marine Geology* 276, 42–57.

Matsumoto, D., Shimamoto, T., Hirose, T., Gunatilake, J., Wickramasooriya, A., DeLile, J., Murayama, M., 2010. Thickness and grain-size distribution of the 2004 Indian Ocean tsunami deposits in Periya Kalapuwa Lagoon, eastern Sri Lanka. *Sedimentary Geology* 230, 3, 95-104.

Meléndez, M.N., Liesa, C.L., Soria, A.R., Meléndez, A., 2009. Lacustrine system evolution during early rifting: El Castellar Formation (Galve sub-basin, Central Iberian Chain). *Sedimentary Geology* 222, 64-77.

Meyer, R., Krause, F.F., 2006. Permeability Anisotropy and Heterogeneity of a Sandstone Reservoir Analogue: An Estuarine to Shoreface Depositional System in the Virgelle Member, Milk River Formation, Writing-on-Stone Provincial Park, Southern Alberta. *Bulletin of Canadian Petroleum Geology* 54, 4, 301-318.

Miall, A.D., 1996. *The Geology of Fluvial Deposits, Sedimentary Facies, Basin Analysis, and Petroleum Geology*. Springer-Verlag, New York, 582 p.

Nanayama, F., Shigeno, K., 2006. Inflow and outflow facies from the 1993 tsunami in southwest Hokkaido. *Sedimentary Geology* 187, 139–158.

Navarrete, R., 2015. *Controles alocíclicos de la sedimentación barremiense en la Subcuenca de Galve (Fm. Camarillas, margen occidental de la Cuenca del Maestrazgo).* PhD Thesis, Univ. de Zaragoza. 444 p.

Navarrete, R., Rodríguez-López, J.P., Liesa, C.L., Soria, A.R., Veloso, F.M., 2013a: Changing physiography of rift basins as a control on the evolution ofmixed siliciclastic–carbonate back-barrier systems (Barremian Iberian Basin, Spain). *Sedimentary Geology* 289, 40–61.

Navarrete, R., Liesa, C.L., Soria, A.R., Rodríguez-López, J.P., 2013b. Actividad de fallas durante el depósito de la Formación Camarillas (Barremiense) en la subcuenca de Galve (E de España). Geogaceta 53, 61–64.

Navarrete, R., Liesa C.L., Castanera D., Soria A.R, Rodríguez-López, J.P., Canudo , J.L., 2014: A thick Tethyan multi-bed tsunami deposit preserving a dinosaur megatracksite within a coastal lagoon (Barremian, eastern Spain). *Sedimentary Geology* 313 , 105–127.

Nishikawa, T., Ito, M., 2000. Late Pleistocene barrier-island development reconstructed from genetic classication and timing of erosional surfaces, paleo-Tokyo Bay, Japan. *Sedimentary Geology* 137, 25-42.

Norden, B., Förster, A., Vu-Hoang, D., Marcelis, F., Springer, N., Le Nir, I., 2010. Lithological and Petrophysical Core-Log Interpretation in CO. *SPE Reservoir Evaluation and Engineering* 13, 2, 179-192.

Pettijohn, F.J., Potter, P.E., Siever, R., 1973. *Sand and sandstone*. Springer-Verlag, New York-Heidelberg-Berlin, 618 p.

Peropadre, C., 2012. *El Aptiense del margen occidental de la cuenca del Maestrazgo: controles tectónico, eustático y climático en la sedimentación*. PhD Thesis, Universidad Complutense de Madrid, 649 pp.

Peropadre, C., Meléndez, N., Liesa, C.L., 2008. Variaciones del nivel mar registradas como valles incisos en la Formación Villarroya de los Pinares en la subcuenca de Galve (Teruel, Cordillera Ibérica). *Geo-temas* 10, 167–170.

Phantuwongraj, S., Choowong, M., 2012. Tsunamis versus storm deposits from Thailand. *Natural Hazards* 63, 31–50.

Pochat, S., Van Den Driessche, J., 2007. Impact of synsedimentary metre-scale normal fault scarps on sediment gravity flow dynamics: An example from the Grès d'Annot Formation, SE France. *Sedimentary Geology* 202, 796–820.

Pyrcz, M.J., Deutsch, C.V., 2014. *Geostatistical reservoir modeling*. Oxford university press, 448 p.

Robinson, J.W., McCabe, P.J., 1997. Sandstone-body and shale-body dimensions in a braided fluvial system: salt wash sandstone member (Morrison Formation), Garfield County, Utah. *AAPG Bulletin* 81, 1267–1291.

Rodríguez-López, J.P., Meléndez-Hevia, N., Soria, A.R., De-Boer, P. L., 2009. Reinterpretación estratigráfica y sedimentológica de las formaciones Escucha y Utrillas de la Cordillera Ibérica. *Revista de la Sociedad Geológica de España* 22, 3-4, 163-219.

Salas, R., 1987. *El Malm y el Cretaci inferior entre el Massis de Garraf y la Serra d'Espadà*. PhD. Thesis, Universidad de Barcelona, 345 pp.

Salas, R., Casas, A., 1993. Mesozoic extensional tectonics, stratigraphy and crustal evolution during the Alpine cycle of the eastern Iberian basin. *Tectonophysics* 228, 1, 33-55.

Salas, R., Guimerà, J., Más, R., Martín-Closas, C., Meléndez, A., Alonso, A., 2001. Evolution of the Mesozoic Central Iberian Rift System and its Cenozoic inversion (Iberian Chain). In: Ziegler, P.A., Cavazza, W., Robertson, A.F.H., Crasquin-Soleau, S. (eds), *Peri-Tethys Memoir 6: PeriTethyan Rift/Wrench Basins and Passive Margins*. Mémoires du Muséum national d'Histoire naturelle 186, 145–185.

Simms, A.R., Anderson, J.B., Blum, M., 2006. Barrier-island aggradation via inlet migration: Mustang Island, Texas. Sedimentary Geology 187, 105–125.

Sohn, Y.K., 1997. On traction carpet sedimentation. Journal of Sedimentary Research 67, 502–509.

Soria, A.R., 1997. *La sedimentación en las cuencas marginales del surco ibérico durante el Cretácico inferior y su control estructural*. PhD Thesis. Universidad de Zaragoza. 363 pp.

Soria, A.R., Meléndez, M.N., Meléndez, A., Liesa, C.L., Aurell, M., Goméz-Fernández, J.C., 2000. The Early Cretaceous of the Iberian Basin (Northeastern Spain). In: Gierlowski- Kordesch,

E.H., Kelts, K.R. (eds), *Lake basins through space and time*. American Association of Petroleum Geologists, Studies in Geology 46, 285–294.

Soria, A.R., Liesa, C.L., Meléndez, A., Meléndez, N., 2001. Sedimentación sintectónica de la Formación El Castellar (Cretácico Inferior) en la subcuenca de Galve (Cuenca Ibérica). *Geotemas* 3, 2, 257-260.

Sugawara, D., Minoura, K., Imamura, F., 2008. Tsunamis and Tsunami sedimentology. In: Tsunemasa Shiki, Yoshinobu Tsuji, K. Minoura, T. Yamazaki (eds), *Tsunamiites - Features and Implications*. Elsevier, Amsterdam, Oxford, 9-50.

Sugawara, D., Goto, K., Jaffe, B.E., 2014. Numerical models of tsunami sediment transport — Current understanding and future directions. *Marine Geology* 352, 295–320.

Sun, S., Shu, L., Zeng, J.C, Feng, Z., 2007. Porosity–Permeability and textural heterogeneity of reservoir sandstones from the Lower Cretaceous Putaohua Member of Yaojia Formation, Weixing Oilfield, Songliao Basin, Northeast China. *Marine and Petroleum Geology* 24, 109–127.

Tye, R.S., 2004. Geomorphology: an approach to determining subsurface reservoir dimensions. *AAPG Bulletin* 88: 1123–1147.

U.S. GeoSupply, Inc., 2015. Wellsite Geological Solutions. Website: www.usgeosupply.com

Veloso, F.M.L., 2015. 3D dynamic modelling of Cretaceous sandstones at the outcrop scale (Galve Subbasin, Iberian Basin). Application to studies of CO2 injection. PhD Thesis, Univ. de Zaragoza. 204 p.

Veloso, F.M.L., Navarrete, R., Soria, A.R., Meléndez Hevia, M.N., 2013. Estudio de afloramiento de escala intermedia como almacén geológico (Aliaga, provincia de Teruel). In: Garcia-Hidalgo, J.F., Gil, Barroso, F. y Diaz de Neira, J.A. (eds). *V Congreso Cretácico de España*, 136-139.

Vennin, E., Aurell, M., 2001. Stratigraphie sequentielle de l'Aptien du sous-basin de Galvé (Province de Teruel, NE de l'Espagne). *Bulletin de la Société Géologique de France* 172, 397–410.

White, C.D., Willis, B.J., Dutton, S.P., Bhattacharya, J. P., Narayanan, K., 2004. Sedimentology, statistics, and flow behavior for a tide-influenced deltaic sandstone, Frontier Formation, Wyoming, United States. In: Grammer, G.M., Harris, P.M., Eberli, G.P (eds), *Integration of outcrop and modern analogs in reservoir modeling*. AAPG Memoir 80, 129-152.

Wood, L.J., 2004. Predicting tidal sand reservoir architecture using data from modern and ancient depositional systems. In: Gramer, M., Harris, P.M., Eberli, G.P. (eds), *Integration of Outcrop and Modern Analogs in Reservoir Modeling*. American Association of Petroleum Geologists Memoir 80, 45–66.

Yoshida, S., Jackson, M. D., Johnson, H. D., Muggeridge, A. H., Martinius, A. W., 2001. Outcrop studies of tidal sandstones for reservoir characterization (Lower Cretaceous Vectis Formation, Isle of Wight, southern England). In: Martinsen, O.J., Dreyer, T. (eds), *Sedimentary Environments Offshore Norway - Palaeozoic to Recent*. NPF Special Publication 10, 233-257. Elsevier Science B.V., Amsterdam.

Highlights

- Facies classified by sand sorting describe better the petrophysics variability.
- Sedimentary process control facies distribution, thus the petrophysics distribution.
- Tsunami deposit has great variation of sand grain size, however sand is well sorted.
- B.i./Inlet deposit has heterogeneous distribution of facies and great variability of porosity.
- Porosity and permeability are strongly correlated in both sandstone deposits.